# Inclusive $\Lambda$ Baryon Spectra in Au+Au Collisions at $\sqrt{S_{NN}} = 200$ GeV

August 7, 2015

By

Dillon Roach

Dissertation

Submitted to the Faculty of the

Graduate School of Vanderbilt University

in partial fullfillment of the requirements

for the degree of

DOCTOR OF PHILOSOPHY

in

PHYSICS

Nashville, Tennessee

Approved:

Professor Senta V. Greene

Professor Charles F. Maguire

Professor Volker E. Oberacker

Professor Richard F. Haglund

Professor David J. Furbish

## Table of Contents

## List of Tables

## List of Figures

# CHAPTER 1

# INTRODUCTION

## 1.1 Foundations and Historical Perspective

As physicists we make it our pursuit to study nature and to attempt to piece together mathematical models of nature's mechanisms. We do this in order to understand more fully the processes around us. In some instances, theories lead us to pursue specific conditions in order to test our models. Other times we stumble upon discoveries quite by accident while pursuing different goals. One particular field that happens to benefit from both scenarios is the study of matter at extreme temperature and pressure. Developing theories about matter have led us to believe that there are places in the universe where these conditions exist to the extent that we may find a new form of matter; places like neutron stars, exploding black holes, the earliest moments of the Big Bang and for the briefest of moments more recently, a laboratory on Long Island, NY. In the pursuit of this new form of matter, extreme conditions are created in ultra-relativistic heavy ion collisions at the Brookhaven National Lab in New York.

In order to access this world of extreme temperature and pressure it is important to understand the particle physics that we use to describe it. Early scattering theories were able to employ perturbation techniques for the relatively weak interactions between leptons, for example, thanks to the small coupling associated with those forces. However, when we begin to concern ourselves with the interactions between nucleons and other particles that interact via the strong nuclear force, and further take those interactions to high energy, particle production can no longer be treated in a similar manner. Acknowledging this in 1950, Enrico Fermi suggested a statistical or thermodynamic model assuming a fully saturated accessible phase space, meaning all possible states are occupied, as a new formalism for modeling these interactions [1].

Isaak Pomeranchuk followed this closely with the addition of an expanding volume and particle freeze-out condition, which predicted particle production proportional to the square root of the center of momentum energy available in the collision [2]. Particle freeze-out has two components; chemical freeze-out, where particle production by inelastic scattering has stopped, and kinetic freeze-out where particle interactions no longer occur and the system has reached a final particle distribution.

Roughly fifteen years later, Rolf Hagedorn, considering what had been learned about hadron resonances, decided to treat the extreme temperature and pressure system itself as yet another excited hadron state, or fireball, no different than the parts that made it up. This hypothesis was a self-consistency check that he applied and he quickly realized that this had strong physical implications as one moved to higher energies. Specifically, he assumed that there must be an exponentially growing mass spectrum based on higher resonances of particles taking part in the collision and from this reasoned the requirement of a maximum temperature that would be related to the inverse slope of that mass spectrum [3]. Using data available at the time he presented an estimate for this critical temperature as $T_0 = (160 \pm 10)$ MeV [4]. The implication of this was that at high temperature hadronic matter would possibly experience a phase transition.

As theories developed and the quark structure of matter was further brought to light, these notions took on new meaning. The Yang-Mills fields [5] put forth in 1954 that describe gluons were used to bind the asymptotically free field theory potentially needed to describe matter under these conditions. This formalism had been developed by Gross and Wilczek and then Politzer two years prior to the Collins and Perry paper [6, 55]. In 1975, Collins and Perry put forth the possibility that superdense matter such as neutron stars, exploding black holes and even the early phases of the creation of the universe might be accessible to "normal physics" [7]. Specifically, at these extreme conditions Collins and Perry posited that matter would

not consist of hadrons, but of the constituent quarks in what they termed a quark soup. Collins and Perry made the claim that within this gauge theory thermodynamic properties could be derived.

Finally, in 1978 after many years of theoretical development in the field, É.V. Shuryak produced a paper that explored a description of the new form of matter that might be produced at the extreme temperatures and pressures described above. Shuryak used quantum chromodynamics (QCD), the field theory that describes strong interactions, as a framework for his study and applied his results to neutron stars as before, but also to hot plasmas in cosmology and to high-energy hadron collisions [8]. Shuryak is also credited with first terming the new phase the quark-gluon plasma (QGP). Some aspects of the QGP require highly non-perturbative calculations and so are not easily solved analytically. However, developments in theory and computing power led to increasing development of a numerical QCD approach that breaks space-time down into discrete parts and is termed lattice QCD. Fig.1 is an example of such a calculation [9] that clearly shows a phase transition as the system temperature passes a critical point. The same paper estimates the critical temperature for the transition as $T_c = 154 \pm 8$ MeV for 3-flavor QCD and $T_c = 173 \pm 8$ MeV for similar 2-flavor QCD. The 2+1 flavor trend represents a calculation assuming two light quarks and a strange quark that is four times heavier, where 2 and 3 flavor calculations represent the number quark flavors.

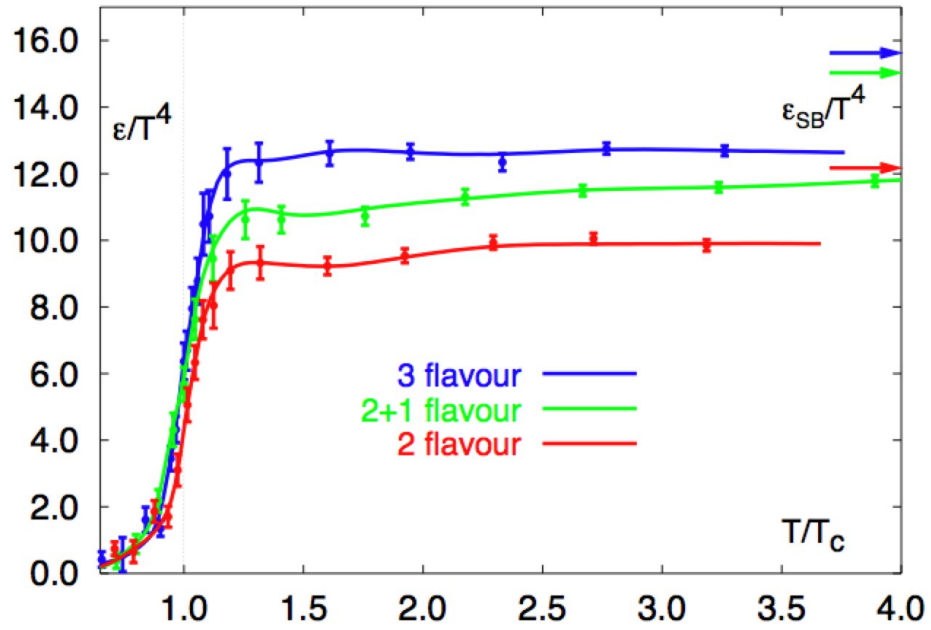


Figure 1: Lattice QCD calculations
These calculations show the phase transition in partonic matter around the critical temperature [9].

### 1.2 RHIC and PHENIX

It is possible to study conditions at these extreme regimes in a laboratory setting at the Brookhaven National Lab (BNL). Located on Long Island, New York, BNL is home to the Relativistic Heavy Ion Collider (RHIC), a collider that is designed to accelerate charged particles and ions around two intersecting rings in opposite directions, bringing them together to collide in one of six intersection regions at center of mass energies per nucleon pair ($\sqrt{S_{NN}}$) up to 200 GeV. In order to reach these energies, the ions being collided undergo a five-stage process before being injected into the final acceleration rings of RHIC. In this process negative ions are first sputtered into the Tandem Van de Graaff, which electrostatically accelerates the ions through a stripping foil giving them a greater positive charge and sending them along to the booster accelerator. For cases where RHIC uses protons in its rings a linear accelerator is the source of the protons and feeds directly into the booster accelerator. Once

in the booster synchrotron, a small, circular accelerator that uses radio-frequency electromagnetic waves for ion propulsion, the particles are accelerated further until they are fed into the Alternating Gradient Synchrotron (AGS). It is the AGS that takes the ions from roughly 37% the speed of light (c) to 0.997 c, after which the ions travel through the final beam line where a switching magnet injects bunches of ions into the RHIC rings. To date, RHIC has run Au+Au, Cu+Cu, U+U, baseline p+p, and d+Au, ranging over several energies from $\sqrt{S_{NN}}$ = 5.0 GeV to 200 GeV.

At four of the six possible intersection regions of RHIC sit the detector systems that actually do the work of retrieving information from the collisions. These four experiments are each made up of many individual sub-detectors and are named PHOBOS, BRAHMS, STAR, and PHENIX. Of the four experiments, PHOBOS and BRAHMS have each completed their missions and are no longer in use. The PHENIX and STAR experiments are still active and are entering their 15th period of data acquisition, known as Run 15. The measurements described in this dissertation were taken using the PHENIX detector.

PHENIX is a spectrometer composed of two central arms perpendicular to the beam pipe and two muon arms at forward and backward rapidity. Rapidity with respect to the beam-axis is defined as $\varphi = \frac{1}{2} ln \frac{E+p_z c}{E-p_z c}$, and its related quantity, pseudorapidity, is $\eta = -ln[\tan(\frac{\theta}{2})]$, where $\theta$ is the angle between the particle momentum $\vec{p}$ and the beam-axis. The coordinate system used in the experiment puts $\hat{z}$ along the beam axis, North, and the azimuthal $\hat{\phi}$ rotates clockwise about that axis in the vertical plane, such that $\phi = 0$ is in the center of the West arm and $\phi = 90^\circ$ points upward. For a schematic drawing of the subsystems and the configuration of the experiment when the measurements described in this dissertation were made see Fig.2 [10]. Further description of the PHENIX detector systems may be found in chapter 2.

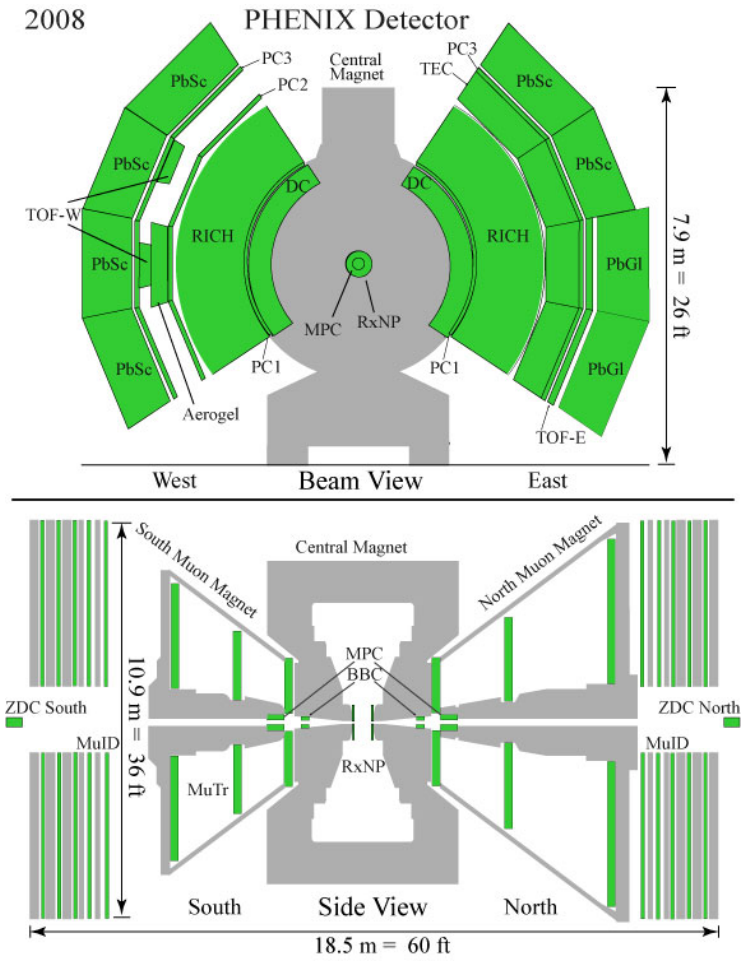


Figure 2: Diagram of the PHENIX detector subsystems

It is the goal of RHIC and PHENIX to produce and determine the properties of the QGP.

### 1.3 Physical Processes in High Energy Heavy Ion Collisions

We claimed the high-density medium could be described by thermodynamic formalisms to a point, but this means that we must justify the use of concepts such as temperature and energy density of the medium as a first step to verifying the existence of the QGP at RHIC.

From general lattice QCD calculations [9] it is expected that the required energy

density to drive a QGP phase transition is around 1 GeV/fm$^3$. Early RHIC results, including those from PHENIX, are presented in the PHENIX white paper [11]. In this, the authors point out that when considering the energy density it is important to know exactly what density we wish to describe. Clearly, they point out, from the perspective of basic special relativity one could boost the system to any arbitrary frame in which basic nuclear matter is Lorentz contracted to the point that it exceeds this density. As well, if we naively assume that the two ions, Lorentz contracted from their RHIC acceleration, nearly overlap in their collision we can also derive densities that far surpass the required 1 GeV/fm$^3$. What is important is the resulting formed particles and their energy density that result from the collision.

In this respect, as a basic model one often refers to the commonly used "Bjorken model" as was put forth by J.D. Bjorken in 1982 in his attempts to make predictions about the QGP, its transition temperature and lifetime [12]. Bjorken predicted an approximate temperature of about 200-300 MeV, which does not fall around the widely accepted $\sim$170 MeV, but his picture of the early system as a disk source of created secondaries between the two passing ions has lived as a paradigm for models to this day. The model is only applicable when the two ions are so Lorentz boosted that they are essentially flat disks themselves, but this is the case in RHIC collisions. See Fig.3 for a diagram of the Bjorken picture.

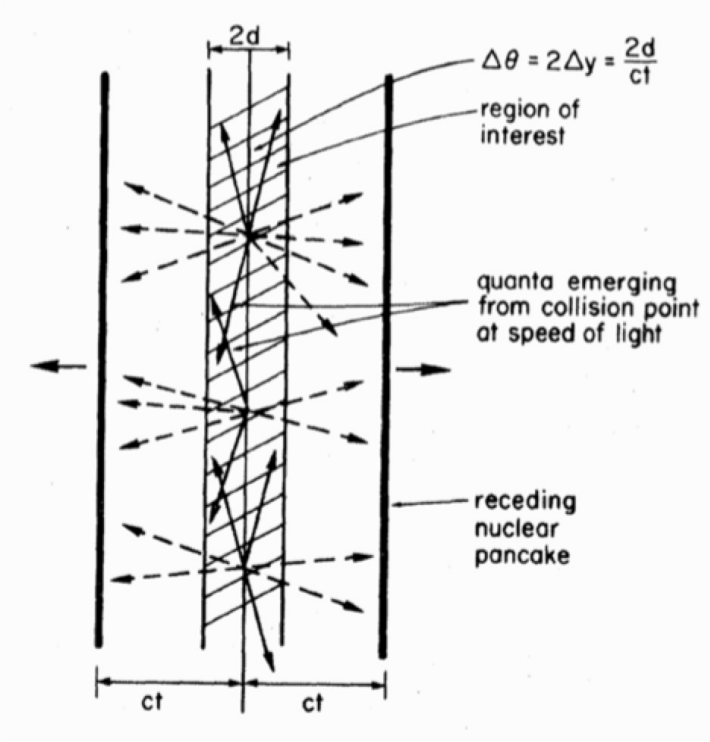


Figure 3: Simple picture of the Bjorken model
In this model particles are emitted simultaneously from the vacuum in between passing heavy ions [12].

The PHENIX white paper uses the basic Bjorken formalism and an estimate of formation time, the time at which a QGP can be considered to have been created, to get an energy density at the time of particle formation. $<\epsilon>$ of 15 GeV/fm$^3$ is presented as an upper estimate for the energy density at the time of formation. This is a conservative prediction and well above the estimated range necessary for the phase transition to QGP, but it is not yet in a state of local thermal equilibrium necessary to apply thermodynamic concepts such as temperature.

In order to derive an energy density at the time of local thermal equilibrium it is first necessary to derive a time scale for that process. Provided the formed particles thermalize quickly it can be estimated $<\epsilon> \sim \frac{1}{\tau}$, and so energy scaling will tend to go as $\tau_{Form}/\tau_{Therm}$, where $\tau_{Therm}$ is the time at which thermal equilibrium is achieved and $\tau_{Form}$ is the time when the first particles in the medium have been formed.

Because of this, the time in which the thermalization process takes place is a good indicator for the energy density relevant to the formation of the QGP. For the time scale in question an approximation for the energy density at thermalization between 5.4 GeV/fm$^3$ and 9.0 GeV/fm$^3$ may be made [11]. Estimates for the thermalization time are addressed in section 1.5.

### 1.4 Particle Production and Hadronization

One key concept is important to define before moving forward: centrality. Heavy-ion collisions do not always occur in such a way that the nuclei perfectly overlap in their collision, it is likely that they should only partially graze each other, or that they should only overlap half way. Centrality is a parameterization of that overlap. Given as a percentage, with 0% indicating perfect overlap and 95% a near miss, centrality is a proxy for the impact parameter b, where b is the distance between the centers of the two nuclei at the time of collision. Collisions that are closer to 0% are referred to as being more central collisions, while those much higher in centrality are termed peripheral.

In the description of the scaling properties between different system sizes, two particularly important and useful concepts are used. $R_{AA}$, or the nuclear modification factor, is the ratio of particle yield in heavy ion collisions to the yield produced from the p+p system as scaled by $N_{coll}$, where $N_{coll}$ is the number of binary collisions, often determined by the Glauber model [18]. The second is $R_{CP}$ or the central to peripheral ratio, defined as the yield ratio between the central and peripheral yields in the same system, each scaled by their appropriate $N_{coll}$. These are defined in Equations 1 and 2.

$$R_{AA} = \frac{dN_{AA}}{N_{coll} dN_{PP}} \tag{1}$$

$$R_{CP} = \frac{dN^{cent}/ < N_{coll}^{cent} >}{dN^{periph}/ < N_{coll}^{periph} >} \tag{2}$$

$R_{AA}$ and $R_{CP}$ are excellent tools for understanding the QGP, because they probe the change to physics processes due to the different pressure and system size of heavy-ion collisions. If the physical processes are essentially the same as a great many single p+p collisions superimposed in space, then the $R_{AA}$ should be equal to one. Any deviation from unity must be understood as either effects relating to the formed hot, dense, matter of the larger collision, or related to differing initial conditions such as those present in highly Lorentz-contracted nuclei. $R_{CP}$ as well as asymmetric collisions, such as d+Au, can be used as tools to differentiate between the hot, dense matter effects and those of the initial conditions.

It is worth noting that when looking at low-$p_T$ d+Au or Au+Au you may see a region where $R_{AA} > 1$. This is a well known feature known as the Cronin effect and is at least partially caused by multiple scattering of the incoming particles before final hard-scattering physics take place and causes a smearing of the appropriate particle $p_T$.

A feature of the particle spectrum in heavy ion collisions that is clearly demonstrated using $R_{AA}$ is high-$p_T$ suppression. Partons propagating through the hot, dense medium undergo energy loss via gluon bremsstrahlung and thereby lose their ability to fragment into high $p_T$ hadrons. This phenomenon, referred to as the high-$p_T$ suppression, is clearly depicted in Fig.4 [23]. For the more central bins, and for minimum bias, the $R_{AA}$ for unidentified charged hadrons, as well as for neutral pions, is strongly suppressed when compared to the single p+p scaling. However, in the most peripheral bins, 60% and greater, this suppression is dramatically reduced. This was a critical discovery with implications for the formation of a hot, dense, strongly-interacting medium. If the mechanism for energy loss is in fact gluon bremsstrahlung as partons traverse the dense medium, not only does this strongly indicate the presence of such

a medium, but also provides a tool for understanding the critical degrees of freedom (hadrons vs partons) in that energy loss through the analysis of different particle species. Different patterns of energy loss for different particles shed light on how each of the partons lose energy and may further provide insight into the formation of final-state hadrons.

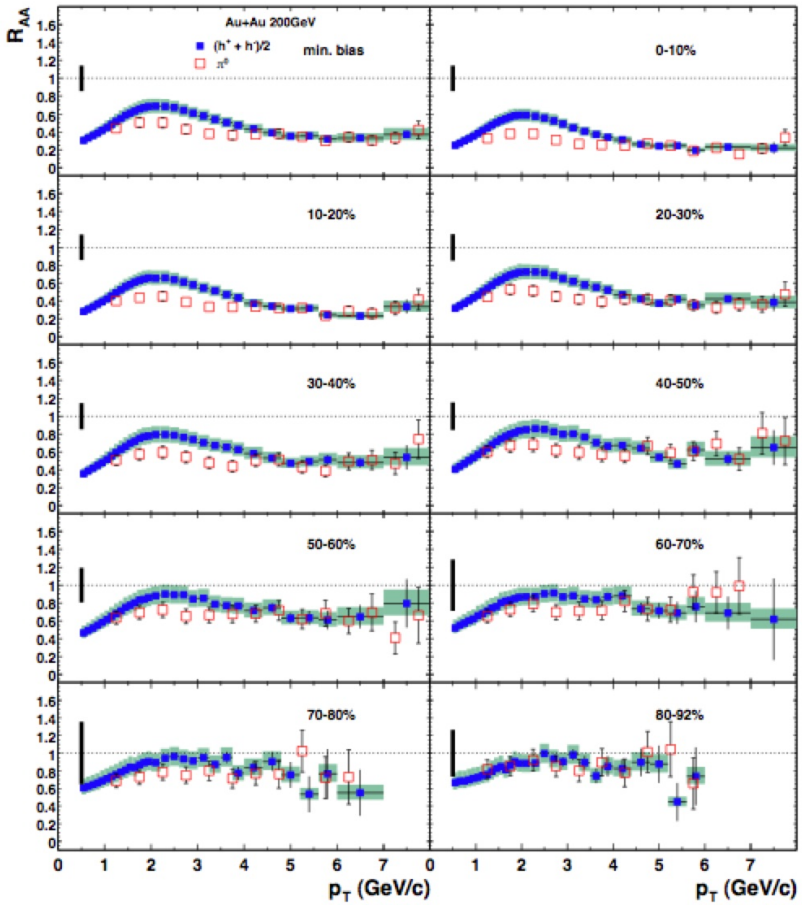


Figure 4: Depiction of the effects of high-$p_T$ suppression
In the dense central collisions parton energy loss lowers the expected yield of particles when compared to the simple binary case of p+p [23].

When looking at particle yields and spectra we note that there is an overproduction of baryons and antibaryons in relation to pions for intermediate $p_T$ between roughly 2.5 GeV/c and 5 GeV/c. As we see in Fig.5 [19], the ratio of protons to pions in central RHIC collisions scales much more quickly than in peripheral collisions. This feature

was not expected ahead of the data and was quite puzzling. One interpretation is that the effect is produced by the mass difference between protons and pions and an in-medium kinematics effect was causing the disparity. As a means to test this, the $\phi$ meson, which has a mass similar to that of the proton, was measured [20]. Surprisingly, while the $\phi$ meson has a similar spectral shape to the proton in $p_T$, the scaling by centrality of the meson followed that of the pion. This scaling is clearly seen in the $R_{CP}$ of the different particles in Fig.6.

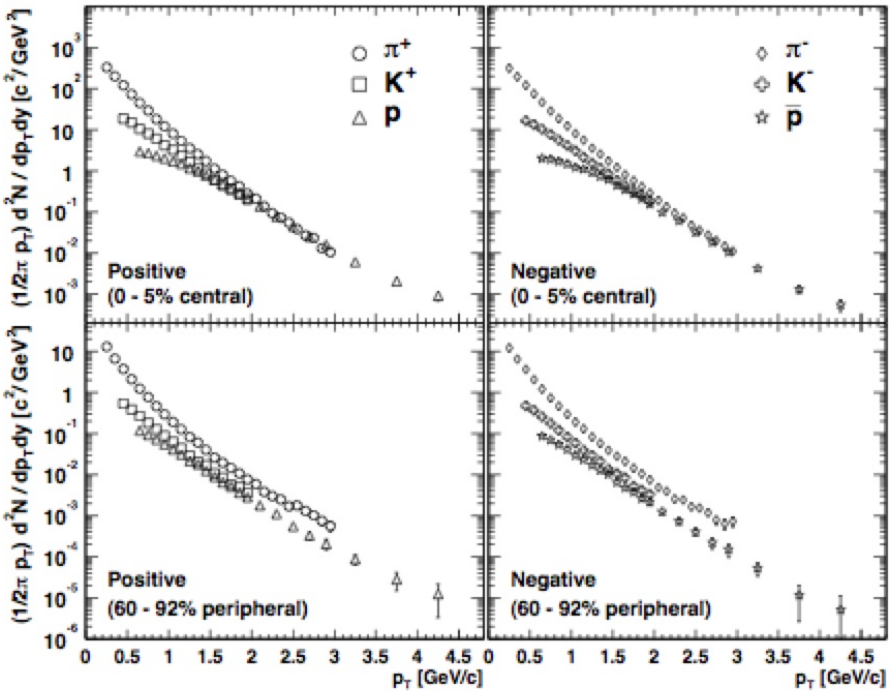


Figure 5: The difference in pion and proton yields as a matter of centrality Over $p_T$, proton and pion yield trend toward each other in the most central bin, while in the peripheral 60-92% they remain distinctly separated [19].

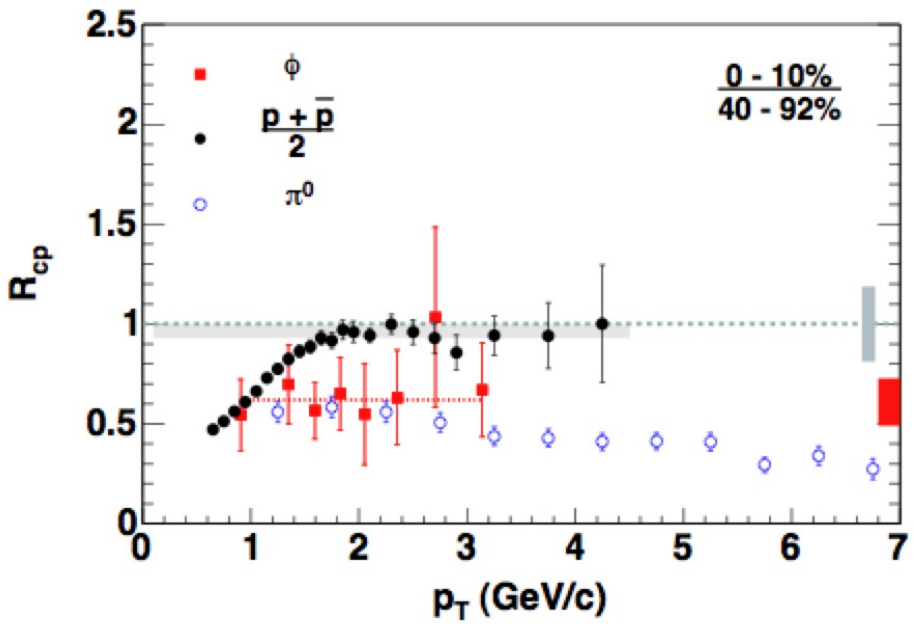


Figure 6: $R_{CP}$ of protons compared to suppression observed for mesons Baryon excess is seen for charge-averaged protons, when compared to both the neutral pion and the $\phi$ meson [20].

This baryon excess, as it was termed, called into question basic assumptions underlying the mechanisms responsible for the hadronization process in the medium. It had generally been assumed that high-energy partons, which are quarks and gluons, in the medium would fragment into particles as the primary means of hadronization, but the baryon excess challenged this assumption. Theories of recombination or coalescence that had been applied to other phenomena in the past were adapted to the particular case of the high-energy heavy ion physics. In a recombination model, quarks come together to form a final hadron state, rather than the high energy fragmentation of partons. A model using thermal parton recombination was suggested by Fries, Muller, Nonaka, and Bass [21]. In this model the recombination mechanism is favored for the intermediate $p_T$ region and fragmentation takes over again at high $p_T$. Another type of recombination theory is proposed by Hwa and Yang of Oregon, in which all forms of hadronization result from recombination [22]. In this Oregon model the high energy partons first fragment into parton showers that later recombine

with other available partons. As we see from Fig.7 [21], inclusion of mechanisms for both fragmentation and recombination can reproduce the data.

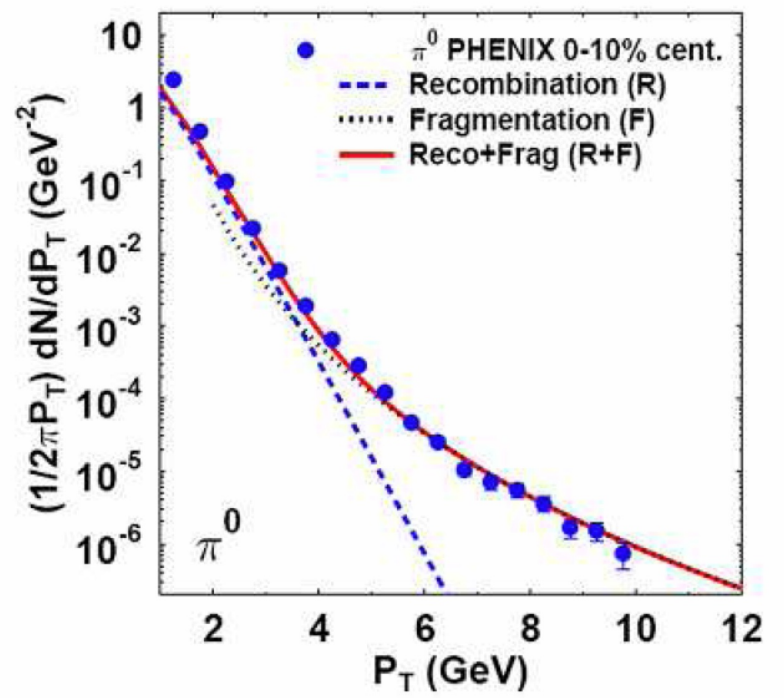


Figure 7: Recombination and fragmentation fits to data
Data is most closely fit by the combination of both fragmentation and recombination mechanisms [21].

### 1.5 Thermalization and Flow

Because of the kinematics of the heavy ion collisions, spatial anisotropies exist in the medium produced by the collisions. For collisions where ions are not perfectly centered with respect to each other, the collision region roughly resembles an ellipsoid where the two ion disks partially overlap as in Fig.8 [10]. Due to this, pressure from strong scattering will drive the system outward with a greater momentum in the minor axis of the ellipsoid which will evolve to a more uniform shape as the system expands and produce an observable flow. The flow affects the azimuthal distribution of observed particle spectra, which can be analyzed using a Fourier expansion [59]. The terms most significant to the flow observed at RHIC are presented here in Equation 3.

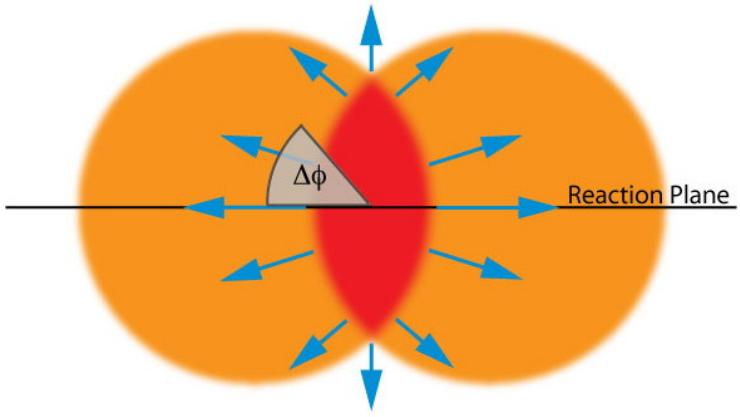


Figure 8: Generalization of a heavy ion collision
In this picture the ions are traveling into and out of the plane of the page, rather than left to right. The intersection region is the area that takes part in the collision. If the two ions were closer together and therefore had a larger overlap this would be considered a more central collision. Alternatively, if they were further apart this would become a more peripheral collision. As well, note the black line drawn across the center of both ions. This is the reaction plane with respect to the page and it always passes through the center of the two ions, such that if we lowered the right ion the reaction plane would be rotated in a clock-wise direction [10].

$$\frac{d^2N}{d\phi dp_T} = N_0(1 + 2\upsilon_2(p_T)\cos(2\phi)) \tag{3}$$

where $\phi$ in this case is with respect to the reaction plane, as shown in Fig.8, and $N_0$ is a normalizaion factor. Ignoring the parton distribution fluctuations within each heavy ion, the expanding system is symmetric about a particular axis, and some terms from the expansion vanish and some survive. The dominating term we observe is the $\upsilon_2$, or elliptic flow of the system and a study of this effect in particle spectra grants us great insight into the early period of the collision fireball. For example, it has strong implications about the validity of hydrodynamic models for the expanding collision system.

A number of hydrodynamic models [13][14][15] attempt to describe the measurements seen in RHIC collisions. In general, these models include parameters that set limits on temperature and thermalization times. At the time of the PHENIX white

paper, all hydrodynamic models that closely resembled the $v_2$ scaling data required the thermalization time to be of the order 0.6-1.0 fm/c, which is the time-scale used to reach the energy density estimates presented earlier. We can further improve our understanding of the medium from flow data when we attempt to discern what exactly is flowing. Clearly, the amount of flow seen in different regions of centrality and $p_T$ give clues to the source of their dynamics, but none so clearly as when we try to scale $v_2$ measurements by the number of constituent quarks in the observed spectra. In Fig.9 [16] we see two sets of graphs; in one set the $v_2$ data is presented in its usual form by transverse momentum, $p_T = \sqrt{p_x^2 + p_y^2}$, or transverse energy $E_T = \sqrt{p_T^2 + m^2}$, while the second set scales these by the number of quarks in the particle species. One possible interpretation is that the flow in the system is taking place while the quarks are able to flow themselves and then when hadronization mechanisms come into play this effect is passed on to the observed particles. This is compelling evidence that quarks and gluons may be appropriate degrees of freedom when describing the hot, dense form of matter.

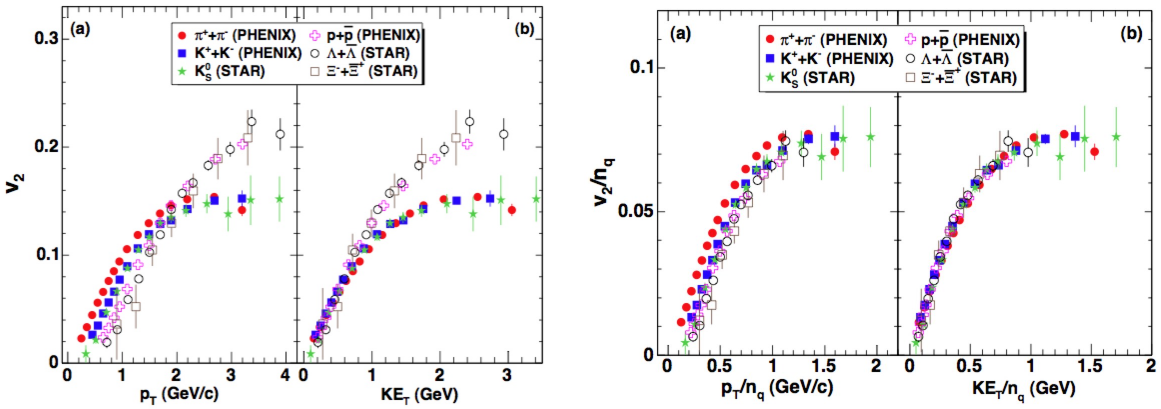


Figure 9: A demonstration of $v_2$ scaling by the number of quarks, $n_q$

It is worth noting that the described $n_q$ scaling does not continue on for all $p_T$; it eventually breaks as particle production mechanism shift and relativistic hydrodynamics are no longer as important to the description of the medium's dynamics [16].

Further successes of the thermal models include their ability to predict particle

spectra seen at RHIC. For a given chemical freeze-out temperature, the point where inelastic collisions cease, particle abundances are affected by the conserved quantities, such as baryon number, charge, and strangeness, and may be modeled using the grand canonical ensemble. The formalism uses parameters for chemical freeze-out temperature, quark chemical potentials which may be different for up/down quarks and for strange quarks, and a free parameter for strangeness enhancement. As an example, Kaneta and Xu [17] apply a thermal model that predicts particle ratios with great accuracy for a number of spectra observed at RHIC, see Fig.10. The particular model puts the value $T_{chem} = 157 \pm 3$ MeV and gives insight into whether chemical equilibrium is achieved in the medium. In these types of models strangeness production plays a key role in determining the amount of chemical equilibrium. In smaller systems such as $e$+$\bar{e}$ or $p$+$\bar{p}$, strangeness production is suppressed due to the available phase-space defined by conserved quantities like baryon number, but as the system size becomes larger, fewer local restrictions are placed on those conserved quantities. As a way of checking chemical equilibrium, the number of strange quarks can be compared to equilibrium calculations and the ratio of these is represented as $\gamma_s$. When the system has reached full chemical equilibrium, $\gamma_s = 1$ as opposed to lower values that imply only partial equilibrium. For the Kaneta model above a $\gamma_s = 1.03 \pm 0.04$ was extracted. This demonstrates how important particle abundances can be for determining the thermodynamic properties of the hot, dense medium.

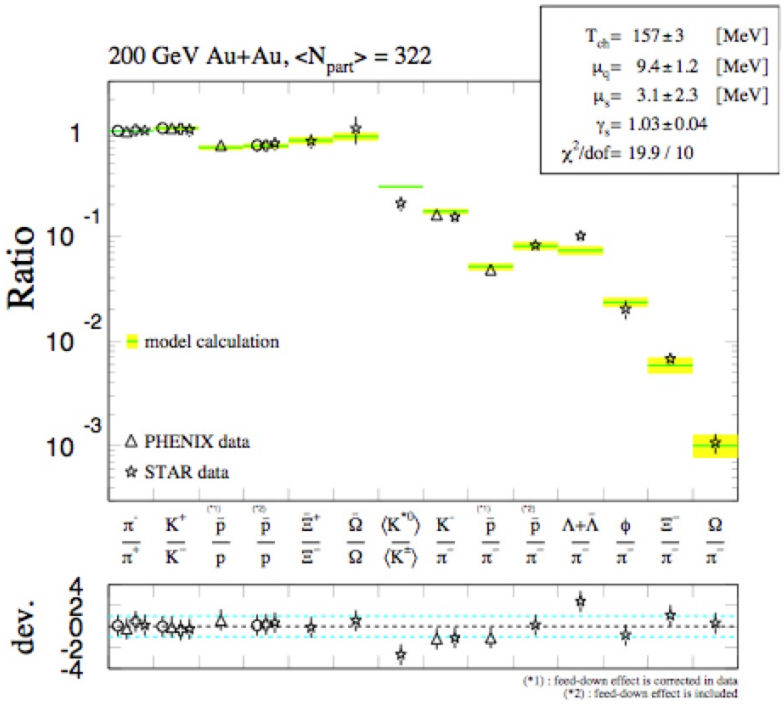


Figure 10: Particle spectra and ratios from PHENIX and STAR described by a thermodynamic model [17].

### 1.6 Lambda and Anti-Lambda Spectra

Previous PHENIX analyses of the lambda baryon spectra have suffered from very low statistics and low PID resolution leading to a low $p_T$ limit on the results. These limits were due to data sets with significantly lower integrated luminosity and the lack of higher precision time of flight detectors. However, with the installation of a new time of flight subsystem starting with Run 7, TOF-W described in section 2, and much greater integrated luminosity, we are able to greatly increase the precision and $p_T$ reach of the analysis. In particular, we are able to provide $\Lambda$ and $\bar{\Lambda}$ spectra in finer $p_T$ binning than was previously possible as well as to reach 7 GeV/c in $p_T$.

The only previously published results on $\Lambda$ and $\bar{\Lambda}$ spectra from the PHENIX collaboration [24] were done at $\sqrt{S_{NN}} = 130$GeV using a data set of 1.3 million min-bias events and covering a $p_T$ range of 0.4 GeV/c to 1.8 GeV/c. This analysis found the $\bar{\Lambda}/\Lambda$ ratio $= 0.75 \pm 0.09$, the $\Lambda/p$ ratio $= 0.89 \pm 0.07$ and the $\bar{\Lambda}/\bar{p}$ ratio $= 0.95$

$\pm$ 0.09. Figures from this analysis are shown in Fig.11; The plot on the far left shows integrated particle yield by $p_T$ for the most central collisions (0-5% centrality) and a scaled minimum-bias spectra that includes all centralities. The middle plot gives the $\bar{\Lambda}/\Lambda$ ratio as a function of $p_T$ (top) and the number of nucleons participating in the collision, $N_{part}$ (bottom). Finally, the plot on the right depicts the lambda invariant mass peak used for signal extraction; an in-depth description of the invariant mass plot and signal extraction process may be found in section 3.

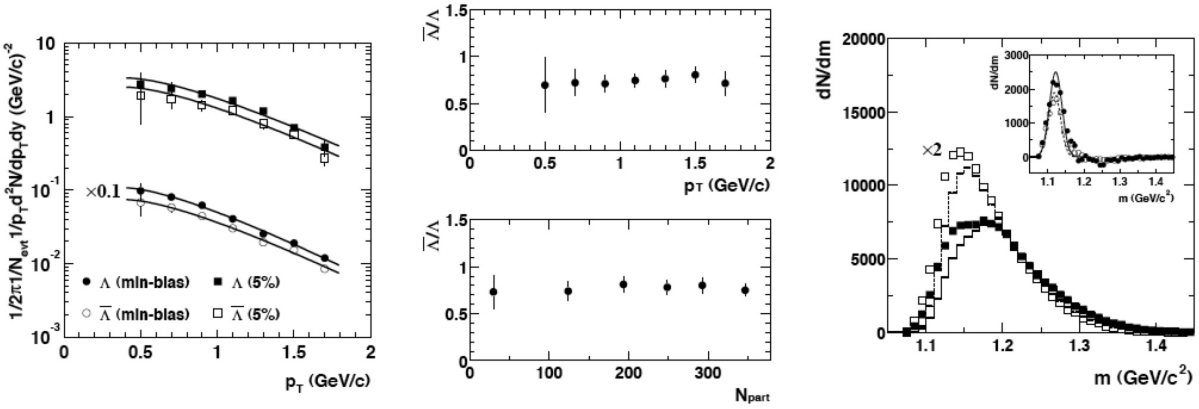


Figure 11: Images from the first PHENIX paper on $\Lambda$ and $\bar{\Lambda}$ spectra
We see here the corrected yields, the particle ratio by $p_T$ and by $N_{part}$ and the shape of the foreground and background with the signal image inset [24].

By contrast, the STAR experiment at RHIC has used lambda, anti-lambda and lambda resonances in several papers. Most relevant to our current discussion are $\sqrt{S_{NN}}$ = 200 GeV p+p spectra to roughly 5 GeV/c [25], $\sqrt{S_{NN}}$ = 200 GeV Au+Au spectra and $R_{CP}$ to roughly 5 GeV/c [26] and a proton-lambda correlation analysis at $\sqrt{S_{NN}}$ = 200 GeV Au+Au [27]. Ref. 25 finds the anti-lambda/lambda ratio = 0.882 $\pm$ 0.017 for p+p data, average $p_T$ and $dN/dy$ at mid rapidity are also presented. More similar to our own study, Ref. 26 presents $\sqrt{S_{NN}}$ = 200 GeV in Au+Au data up to 5 GeV/c $p_T$; in this paper they not only find integrated yield dN/dy by centrality, but also strangeness equilibrium as having been achieved in central RHIC collisions and baryon excess for hyperons, including the lambda, which fits well with models of

hadron formation using quark recombination. More recently, STAR has also published a strangeness enhancement paper that includes $\Lambda$ and $\bar{\Lambda}$ results out to $p_T = 7.5$ GeV/c [28]. Our results are compared with the findings in their latest study. Results from Ref. 26 are presented in Fig.12.

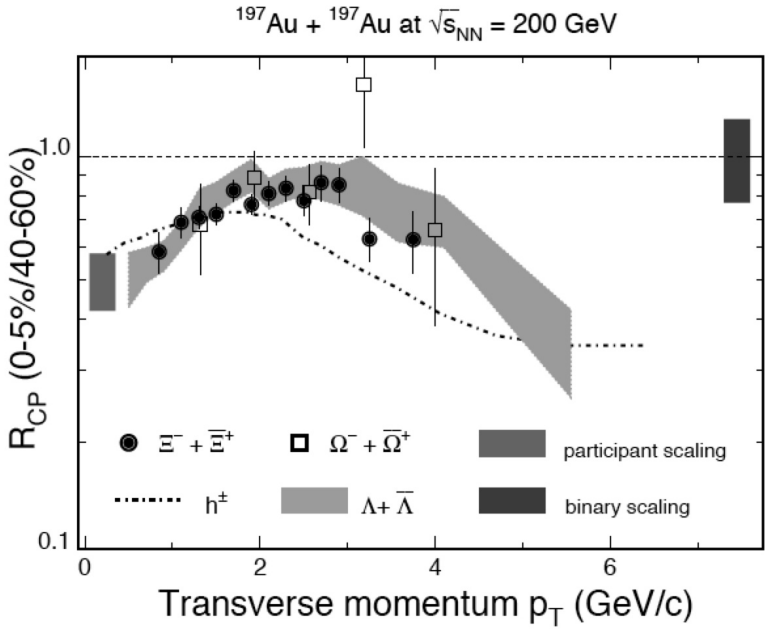


Figure 12: $R_{CP}$ measurement by STAR of hyperons demonstrating baryon excess This structure of the measurement supports a recombination model of hadronization [26].

Our new lambda measurement goes well beyond previously published PHENIX results and matches the $p_T$ reach published by the STAR collaboration. In contrast with the 1.3 million events used for the original PHENIX lambda publication, our current analysis has access to roughly 4.5 billion events. The improved binning and $p_T$ reach allow us to evaluate particle production models, address the effects of strangeness enhancement, and compare to the measurements published by the STAR collaboration.

# CHAPTER 2

# RHIC AND PHENIX

## 2.1 Overview

The Relativistic Heavy Ion Collider (RHIC) is located at Brookhaven National Lab (BNL), in Upton, New York. RHIC is a particle collider that is designed to accelerate charged particles and ions around two intersecting rings in opposite directions, bringing them together to collide in one of six intersection regions at center of mass energies per nucleon pair up to $\sqrt{S_{NN}}$ = 200 GeV or up to 500 GeV in the case of proton-proton collisions. At four of the six possible intersection regions in RHIC sit the detector systems that actually do the work of retrieving information from the collisions. These four experiments are each made up of many individual detectors and are named PHOBOS, BRAHMS, STAR, and PHENIX. Of the four experiments, PHOBOS and BRAHMS have each completed their missions and are no longer in use. The remaining experiments, PHENIX and STAR, are still very active and are currently in their 15th period of data acquisition, known as Run 15. PHENIX, or the Pioneering High Energy Nuclear Interaction eXperiment, is a spectrometer composed of two central arms in the central rapidity region and two muon arms at forward and backward rapidity.

Before entering RHIC, particles pass through a series of smaller-scale accelerators. For the case of Au+Au, a beam of gold ions is produced in a pulsed sputter ion source. The Tandem Van de Graaff accelerator receives ions with a negative charge of Q = -1. The gold ions are accelerated from ground to a +14 MV potential and pulled through a stripping foil in the high-voltage terminal of the Van de Graaff. The ions were initially negatively charged and pulled toward the foil. However, they lose electrons as they pass through the foil, becoming positively charged, and now see the +14 MV potential as a repulsive force, which further accelerates the ions toward the exit of the

Tandem. As the gold ions leave the Van de Graaff, they have charge Q = +12 and kinetic energy of roughly 1 MeV/u, where u is the atomic mass unit, 931 MeV/$c^2$, slightly less than the mass of a proton. The ions are stripped by another foil to Q = +32 and passed to the booster synchrotron, which accelerates the ions further to 95 MeV/u. Yet another foil at the exit of the booster synchrotron strips away all but 2 electrons per atom, leaving the ions at a Q = +77 state as they are passed to the Alternating Gradient Synchrotron (AGS). The AGS is the final accelerator the ions enter, prior to being injected into the RHIC rings. In the AGS, the ions are controlled into bunches that will remain grouped together throughout the remainder of their journey through RHIC, and are accelerated to 8.86 GeV/u. Upon leaving the AGS, the gold ions are stripped of their final electrons, now Q = +79, and injected into the storage rings of RHIC.

## 2.2 RHIC Description

RHIC [51] is an intersecting storage ring collider with 396 dipole and 492 quadrupole magnets responsible for focusing and bending the two beams. When running gold at $\sqrt{S_{NN}}$ = 200 GeV the dipole magnets operate at 3.458 T. The magnets are superconducting and require temperatures below 4.6 Kelvin, using helium refrigerant. Radio-frequency systems operating at 28.15 MHz are utilized for the capture of the injection beam, acceleration, and control of the initial bunch shape. The beams are accelerated by the 28.15 MHz RF systems and then passed to 197 MHz storage RF systems mostly responsible for maintaining a bunch-length size of <30 cm rms. Over time beam luminosity is lost to intra-beam scattering and other mechanisms; a given beam is typically circulated in the storage rings for roughly 10 hours before the beam is deemed no longer ideal for data taking rates and is safely dumped from circulation. RHIC was designed to be able to accelerate different species of particles and has been used to accelerate protons, deuterons, gold, copper, and even uranium (interesting for

its oblong, football, shaped nucleus). RHIC is also capable of accelerating asymmetric species, such as deuterons+gold (d+Au) and copper+gold (Cu+Au). For a full list of energy and species combinations that had been collided previous to our analysis, Run7, see Table 1.

| RHIC Run | Species | Collision $\sqrt{S_{NN}}$ |
|---|---|---|
| 1 | Au+Au | 130 GeV |
| | Au+Au | 56.0 GeV |
| 2 | Au+Au | 200 GeV |
| | Au+Au | 19.6 GeV |
| | p+p | 200 GeV |
| 3 | d+Au | 200 GeV |
| | p+p | 200 GeV |
| 4 | Au+Au | 200 GeV |
| | d+Au | 62.4 GeV |
| 5 | Cu+Cu | 200 GeV |
| | Cu+Cu | 62.4 GeV |
| | Cu+Cu | 22.5 GeV |
| | p+p | 200 GeV |
| 6 | p+p | 200 GeV |
| | p+p | 62.4 GeV |
| 7 | Au+Au | 200 GeV |

Table 1: RHIC run energies and species

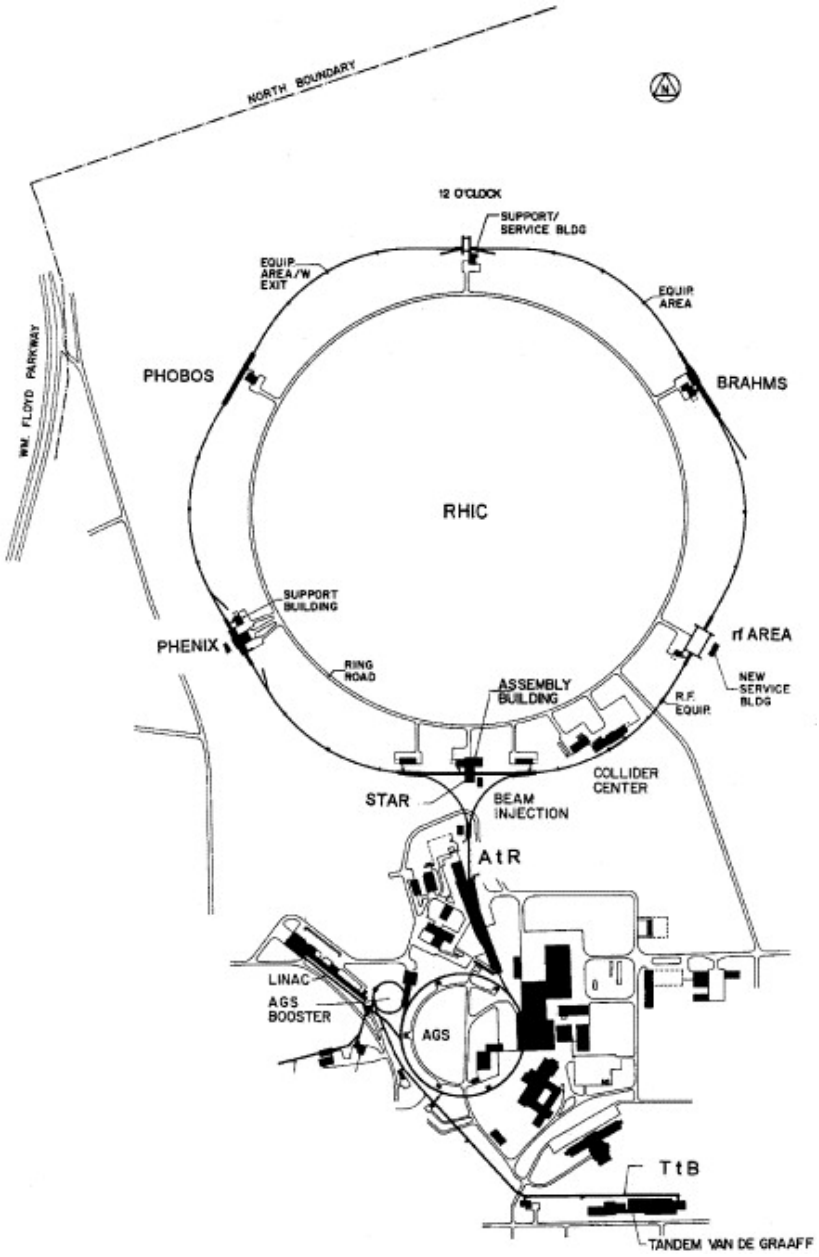


Figure 13: Diagram of the RHIC Complex [51]

## 2.3 PHENIX

A PHENIX [52] event is a single collision between two particles or ions that we may wish to record. PHENIX is a collection of subsystems and the Beam Beam Counters (BBC) come into play first, acting as the start timer and partially determining the location and centrality of the collision. Further away from the main detectors, up and

down the beam tunnel from the intersection region, are the Zero Degree Calorimeters (ZDC). In every event the ions are not assured to overlap completely; they may overlap partially and so not all of the two ions take part in the collision. The ZDCs collect the parts of ions that are left over and not directly involved in a collision, thereby recording information that may be used to infer what part of the ion was involved in the collision. This measurement, along with the BBC information, helps define a value we term centrality. By definition 0% centrality is complete overlap, like stacking two plates on top of each other, whereas 90% centrality implies that the two ions merely grazed each other, a small fraction of their nucleons taking part in the collision.

For a recorded event, the remaining detectors are used to glean as much information from the collision as we possibly can. In the muon arms sit the Muon Trackers (MuTr) and the Muon Identifiers (MuID), which identify muons and record their positions and momentum. In the central arms the Drift Chambers (DC) come first, recording hit information used to reconstruct position and momentum of the tracks as they leave the collision, followed closely by the first Pad Chambers (PC1) which record the track position directly after the DC. Further out sit another set of Pad Chambers (PC3), which also take part in determining the charged particle paths; this process is known as tracking. Only in the west arm, the Pad Chambers have an extra set of chambers located between PC1 and PC3, referred to as PC2. Of note, the pad chambers and drift chambers require the tracks to have electric charge and so are blind to any neutral particles that may cross their acceptance.

In addition to tracking, the central arms also provide very good particle identification. The Ring Imaging Cerenkov (RICH) is designed to identify electrons. The Electromagnetic Calorimeter (EMCal) is excellent for measuring photons and electrons as well, but also has modest particle identification (PID) capabilities up to around 2.5 GeV/c in transverse momentum ($p_T$). The Time of Flight East (TOF-E),

and Time of Flight West (TOF-W) provide high-precision timing information that may be combined with information from the Pad Chambers and the Drift Chambers to determine charged hadron identification. The TOF-W, which was built and installed mainly by the group at Vanderbilt, began operation in Run 7 and has PID capabilities extending to 6 GeV/c in $p_T$. Along with the Aerogel Cerenkov Counter (aerogel), which provides particle distinction at high $p_T$ ranges, the TOF-W is designed to be able to provide PID function toward 10 GeV/c in $p_T$.

For a schematic of the subsystems and the general layout of the experiment see Fig.14.

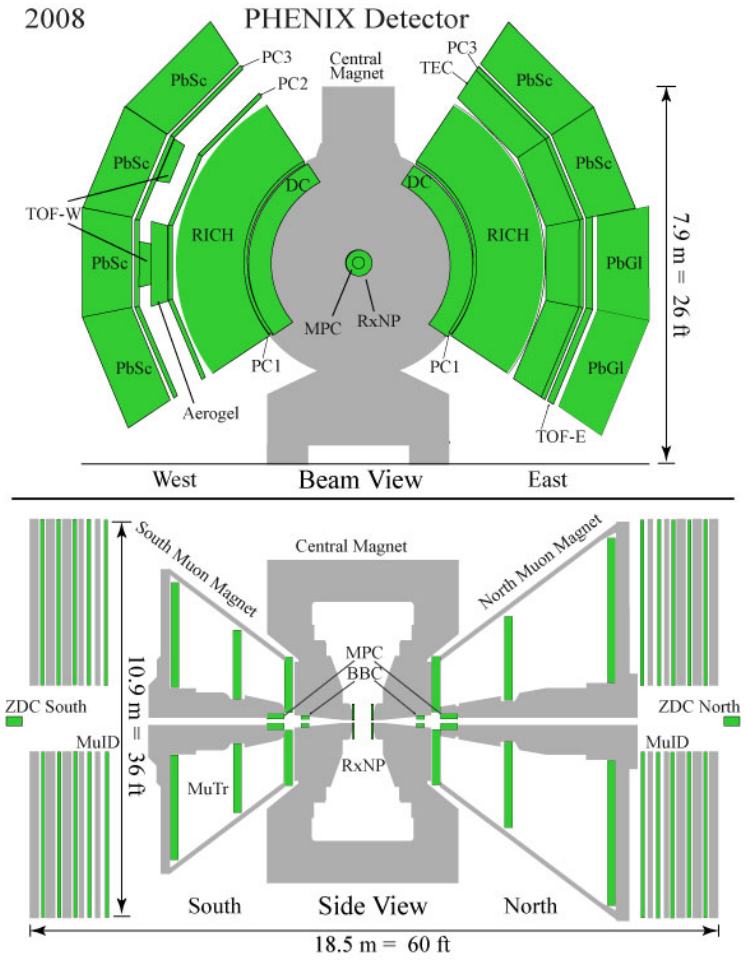


Figure 14: Reproduction of Figure 2, Diagram of the PHENIX detector subsystems.

### 2.3.1 Beam/Beam Counters

For the purpose of detecting the first signs of a collision, or the start of an *event*, so that PHENIX can determine the start point for a particular collision, both in time and in space, the Beam/Beam Counters (BBC) [29,53] are employed. The BBC consists of two separate clusters of 64 detector elements that sit along the beam pipe 1.44 m north and south of the interaction point. In either cluster the BBC covers an angle of 2.4° to 5.7°, or a pseudorapidity of $3.0 < \eta < 3.9$. The BBC is required to be very precise in its timing accuracy, and also to be able to withstand very large amounts of radiation coming from the collision products as well as background associated with the beam itself. When fast-moving, charged particles pass through the 3 cm fused quartz at the front of each detector element in the BBC, they produce Cherenkov light. Photomultiplier tubes are coupled to each quartz radiator element and detect the produced light, creating a signal that is read out by the subsystem's electronics. Each of the two segments of BBC, north and south, register the timing of the first charged particles coming from the collision byproducts. Taking the timing average from both segments gives the event start time, while the difference in arrival times at north and south provides a collision location along the beam-pipe axis. The BBC as a whole has an intrinsic timing resolution of 100 ps as measured in test experiments, but can be improved to 50 ps by standard slewing corrections.

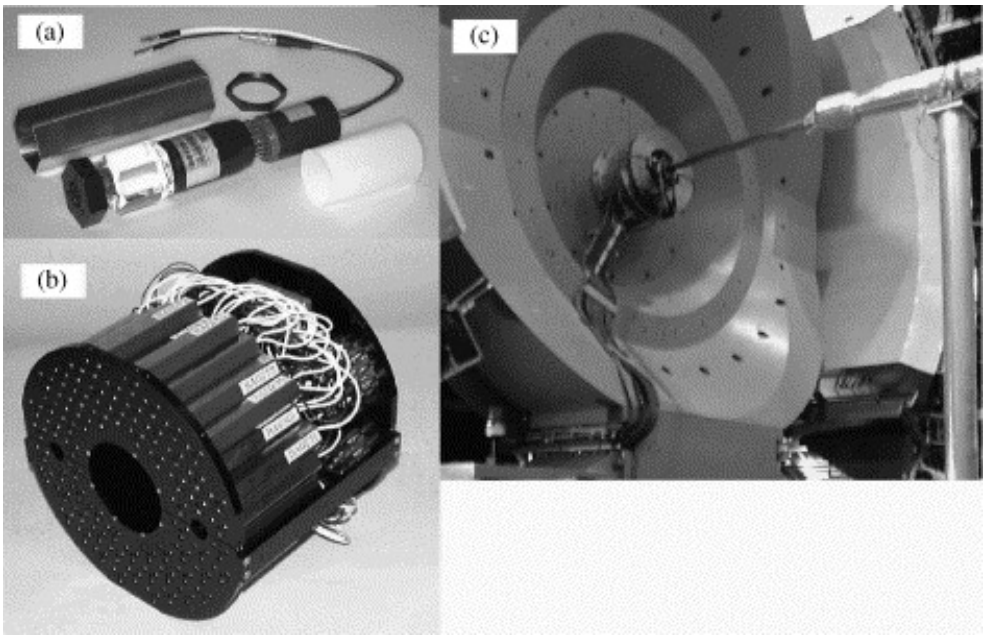


Figure 15: Photographs of the BBC
a) An individual BBC quartz radiator and photomultiplier; b) constructed array of 64 BBC elements; c) one set of 64 BBC elements installed along the beam-pipe in PHENIX [29].

### 2.3.2 Drift Chambers

The first detector subsystem a particle will encounter as it traverses the PHENIX central arms is the Drift Chamber (DC) [30,54]. The drift chambers are two independent arcs, one in each central arm, positioned roughly 2m from the beam pipe. In essence, the drift chambers are large volumes of 50-50 argon-ethane gas mixture contained in a structure with a large number of wires inside. When charged particles pass through the gas volume they ionize the gas, which is then detected by sense wires inside. The purpose of the DC is to participate in the reconstruction of particle track trajectories through the rest of the PHENIX central arms, which is in part used to determine the momentum $p$ of a charged particle passing through. The active area in each of the drift chambers covers 90° in azimuth and $-0.35 < \eta < 0.35$ in pseudorapidity, 1.8 m along the z-axis. Each drift chamber contains 3200 sense wires, for a total of 6400 between them, which are read out at either end of the wire. These wires are broken

down into six different modules X1, U1, V1, X2, U2, V2, as they are ordered radially along r. The X designations contain wires that run along the z-axis, parallel to the beam pipe, and give the location of a track in the azimuth. The U and V modules contain wires that are at small angles to the beam pipe and can thereby resolve the z-axis coordinate of a track passing through. The sense wires are the anode wires in the drift chambers, but there are also cathode, gate, potential, and back wires. The back wires protect nearby sense wires on one side from ionization electrons from other tracks on their side. The potential wires decouple adjacent sense wires, and the gate wires limit drift path length in the chamber.

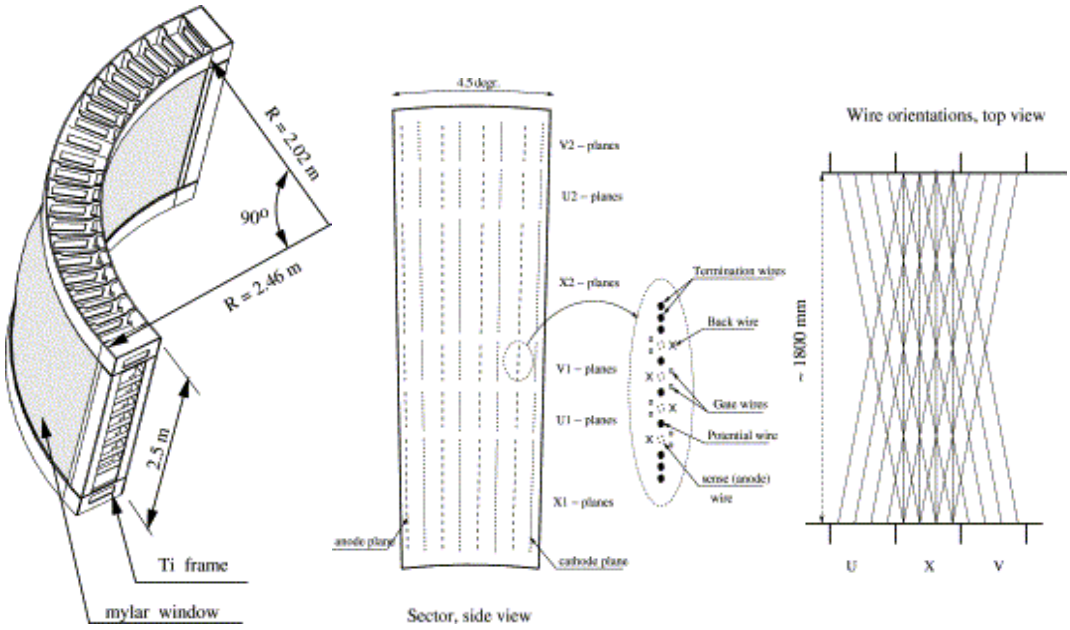


Figure 16: Diagrams for the DC structure (left) and wire construction scheme (center, right) [30]

### 2.3.3 Pad Chambers

The Pad Chambers (PC1,2,3) [30,31] are multiwire proportional chambers and are crucial in determining the positions of charged particles as they pass through PHENIX. The pad chambers are broken into 3 separate groupings. The PC1 group consists of 8 chambers per arm, are 0.5 m x 2 m each, and are mounted directly behind the drift

chambers to give a position immediately after a particle has exited the drift chambers. The position resolution for the PC1 has been measured at $\pm$ 1.7 mm along the z-axis, while the resolution between wires is roughly $\pm$ 4 mm. The PC3 group are the furthest away from the beam pipe and are scaled to cover the same pseudorapidity and azimuth as the PC1 group, while the PC2 group (which is only installed in the West arm) sits between PC1 and PC3. Together, the pad chambers provide a number of three-dimensional position points for a given charged particle as it travels outward from the initial collision. The pad chambers, like the drift chambers, are reliant on a volume of gas that is ionized by charged radiation passing through it. The gas system for the pad chambers is shared with the drift chambers and is essentially a 50-50 argon-ethane mixture, though in the later years of operation it has been necessary to add in ethyl alcohol to help suppress unwanted discharges inside the chambers, thus reducing radiation damage. Inside the volume of gas sit a plane of wires, both field and anode, which move the ionized gas into the cathodes of the detector, one plane of which are arranged in pixels. When the charge in the gas is collected in a particular cathode pixel, this is read out to electronics outside of the chambers, first to a read-out-card (ROC) and then eventually to a front-end-module (FEM) which formats the information for transmission via optical cable to the data counting house. By matching the position hits in the pad chambers with the expected projections given by the drift chamber and PC1 hits, the PHENIX reconstruction software is able to build likely particle trajectories and to reject detector signals caused by secondary particle production in detectors as well as any low-momentum tracks which curl back around in the detectors magnetic field, hitting detectors again. For the PC1, efficiencies above 99% are obtained with anode high voltages above 1675 V, while PC2/3 operate beyond 99% efficiency above 1875 V. A discriminator threshold governs the readout of each of the PC pixels. However, a common problem for discriminator readout is the introduction of false hits produced by electronics noise. For the pad

chambers this is addressed by segmenting a particular pixel into a set of 3 smaller elements, and then requiring that any registered particle hit have a coincidence between all 3 sub-elements. The resulting set of 3 pixel elements is termed a cell. An obvious drawback of segmenting each pixel into 3 is that the number of outputs that must be read jumps as well. For the pad chambers this is addressed by connecting 9 individual pixels together in a configuration seen in Fig.17, on the left. This set of 9 connected pixels is termed a pad and gives rise to the name of the detector subsystem. By arranging pads so that they overlap as seen in Fig.17 any given cell of 3 pixels is uniquely defined by a specific collection of pads. This design saves a factor of 3 in readout channels compared to a design where each individual cell is given its own channel, and a factor of 9 compared to the case where each pixel in every cell is read out separately. This geometric trick is easily my favorite thing about the pad chambers' design.

While working in PHENIX as a Vanderbilt student I was tasked with aiding the operation and wellbeing of the pad chambers as a subsystem expert. As a subsystem expert I spent over 365 days living at Brookhaven National Lab, split between trips. While onsite at BNL I worked with shift crews, physics and engineering staff, and senior physicists to ensure the smooth startup, everyday running and repairs of the pad chambers throughout a physics run. During a run this typically took the form of smaller-scale hardware repairs, fielding questions from shift crews, and minor software upkeep for the particular subsystem. Between yearly physics runs, when the PHENIX detectors were not needed for operations, subsystem expert duties included larger scale repairs, software updates, and any troubleshooting or diagnostics which were not easily accomplished in the middle of collider operations. I am indebted to the excellent group of people regularly at PHENIX who helped me in this sometimes-challenging task and principally to Dr. Anders Oskarsson of Lund University who was a constant guide and voice of authority for everything pad chambers.

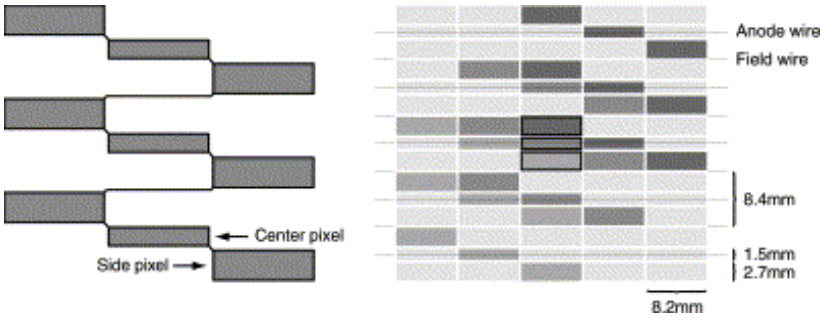


Figure 17: Diagram of PC pad design and organization
Designed to cut down on noise and the number of required electronic readouts, while retaining good spatial resolution, the pads form the cathode for the pad chambers [30].

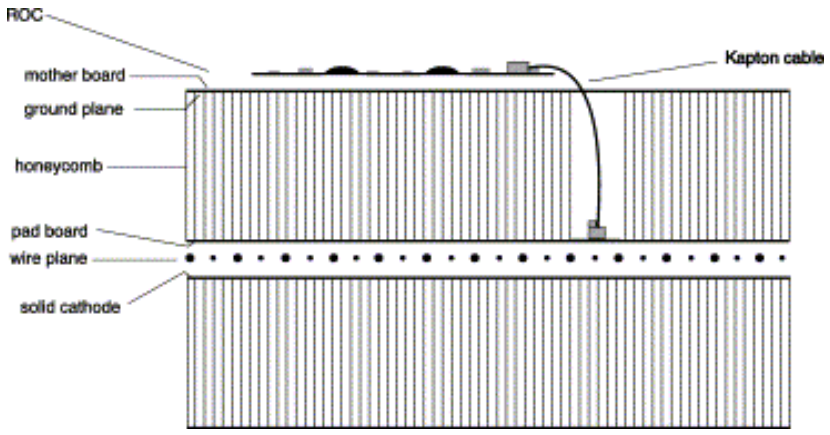


Figure 18: Side cut-away schematic for the pad chamber construction
The read-out-card (ROC) sits outside the gas volume [30].

### 2.3.4 Time of Flight West

The Time-of-Flight-West detector (TOF-W) [32] was installed in PHENIX in June of 2006, shortly before 2007 data taking (Run7). The purpose of the TOF-W is to provide a high-resolution timing measurement for charged particles. The TOF-W provides the stop time to the BBC's start time measurement and the two subsystems collectively provide a 79 ps effective timing resolution. When subtracting in quadrature the BBC's roughly 40 ps start-time resolution, the TOF-W is found to have an intrinsic timing resolution of 69 ps. The TOF-W is installed 480 cm from the beam axis, just before the PC3 in the west arm, and consists of 4 identical metal chambers,

each measuring 192.4 cm x 92.6 cm x 7.5 cm. The TOFW is installed in PHENIX in two pairs of chambers. Both pairs are end-to-end along the z-axis, covering the width of the central arm, $|\eta| < 0.35$. One pair of chambers covers azimuthal angle –6.3° (0.110 rad) $< \phi <$ 3.5° (0.61 rad), while the other is higher up at 16.2° (0.283 rad) $< \phi <$ 26° (0.454 rad), allowing for back-to-back correlation studies with the previously installed time-of-flight-east (TOF-E). At its heart the TOF-W is another gas chamber meant to detect charged particles via ionization induced in the gas as charged particles traverse the volume. The freed electrons are accelerated by a large voltage difference, causing an avalanche effect. To that end the TOF-W is filled with a 90% Freon (C2F4H2), 5% isobutene (C4H10), 5% Sulfur Hexafluoride (SF6) gas mixture and held at a 14 kV potential difference (+7 kV, -7 kV). Where the TOF-W differs from a simple gas chamber detector is the use of 32 multi-gap resistive plate chambers (MRPC) within each larger volume, for a total of 128 between the 4 main chambers. Inside a given MRPC are six 230 mm gas planes, each separated by one of the five 550 mm resistive glass plates in the MRPC. Instead of seeing a single large gas volume, a charged particle now passes through 6 separate small ones. The small gas layers limit the size of the avalanche and minimize the inherent statistical variations in the layout. In exchange for reduced noise and cleaner signal resolution a single, a small gas-layer has a relatively small signal amplitude, which is why multiple layers are stacked vertically and their combined signal is read out. The produced avalanche in the gas layers is collected on one of four copper strips in each MRPC. Each of the strips is read out at both ends and the timing difference between one end and the other is used to locate the track position in reference to the middle of the strip by $DY = \frac{(T_{up} - T_{down})}{2} V_{signal}$, where $V_{signal} = 16.784$ cm/ns and is the signal propagation speed along the strip.

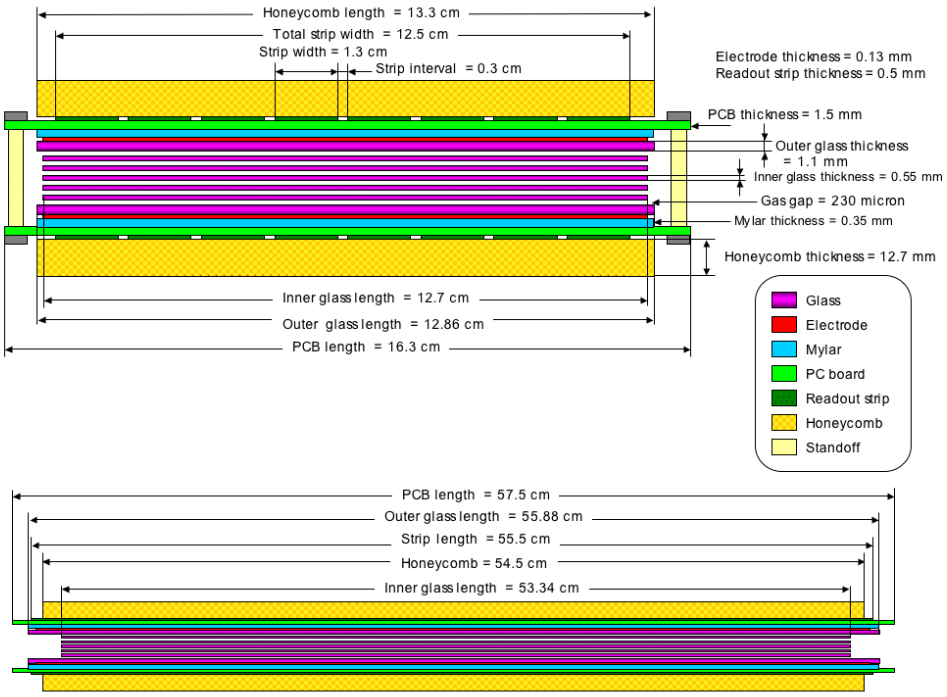


Figure 19: Design and measurements for the TOF-W MRPC [32]

# CHAPTER 3

# MEASUREMENT DETAILS

This section describes the process for our study of the lambda baryon spectra in Au+Au collisions at $\sqrt{S_{NN}}$ = 200 GeV using Run7 data through the $\Lambda \rightarrow p + \pi^-$ decay channel, detected in the PHENIX central arms. For the anti-lambda baryon the decay is $\bar{\Lambda} \rightarrow \bar{p} + \pi^+$. The study of the lambda baryon in PHENIX is complicated by its relatively long lifetime, roughly $2.63 \cdot 10^{-10}$ seconds. Because PHENIX tracking at the time of Run7 had no way of determining the secondary vertex of a decay, all tracks are assumed to have originated from the reconstructed collision vertex. For the case of the lambda's daughter particles, which may be created far away from the collision vertex, this procedure can lead to particle momentum misreconstructions. In part to compensate for this fact, we analyze the lambda spectra using two different methods. In one case we place no particle identification constraints on either daughter particle and reconstruct the lambda by combining positive and negative tracks in the PHENIX central arms. In the other method, we use the time-of-flight-west (TOF-W) detector for identification of the proton and combine that with a negative track from the west arm. By including the TOF-W, we trade the improved accuracy of identifying one daughter particle for a loss in overall statistics available, because of the smaller acceptance of the TOF-W when compared to the entire west arm.

## 3.1 Data Selection

In PHENIX our data is stored in thousands of files which contain the variables for a given set of events, broken into what are referred to as runs. Not to be confused with the yearly designation of the collider operations, such as Run7, in this case a *run* is typically defined by one continuous data capture and roughly contains the selected collision events that were recorded over the course of one hour. For our study we

analyze minimum bias, post-production data files, meaning only the most general event trigger is required to capture an event and files are formatted in such a way that processed variables are directly available to analyzers. Each file is given a run number, where Run7 started in the 228000s, we start analyzing data after run 229000 and we reject the following runs based on magnetic field configuration:

235889< Run Number < 236009

Run Number = 229545, 231156, 236137, 238530, 238531, 238971, 239312

For Run7, the PHENIX central magnet system, designed to bend charged particle trajectories for charge and momentum reconstruction, primarily ran under two configurations. Referred to as $+-$ and $-+$ field, based on the system's two concentric coils that are able to run current in either direction, the field configurations will bend charged particle trajectories along $\hat{\phi}$ depending on the charge of the particle. The runs below 235811 have a $+-$ magnetic field configuration (field lines going from positive to negative $\hat{z}$), while those after 236132 are $-+$ field runs (negative to positive $\hat{z}$ field lines); we analyze these two sets of data separately as a means of cross-checking our results and expect the corrected measurements to agree within uncertainties. The number of events analyzed for the $+-$ field configuration is $2.0289 \cdot 10^9$ and the number of events for the $-+$ field configuration is $2.1831 \cdot 10^9$. For each event, we reconstruct $z_{vertex}$, the location of the collision along the beam-pipe, where $z_{vertex} = 0$ coincides with the center of the PHENIX experiment. We require that events be within $|z_{vertex}| < 30$ cm for analysis. Particles originating outside this range may not be reliably reconstructed or analyzed.

### 3.2 Track Selection

For tracking and identification, this analysis uses the drift chamber (DC), the pad chambers (PC1, PC3), and the time-of-flight-west (TOF-W). In PHENIX all data is run through production software before being made available to individuals for anal-

ysis. This process runs calibrations and adjustments that are data-quality related so that the variables a given collaboration member sees in the data have already been corrected for basic hardware level adjustments. More significantly, the PHENIX production software processes individual hits throughout the detectors and builds particle trajectories that match a given set of detector hits. These particle trajectories are called tracks and are based on a projection from the reconstructed collision vertex outward through hits in the drift chambers and pad chambers. Each track reconstructed in this manner is tagged with a drift chamber quality value, essentially describing the likelihood that the given track belongs to a unique, well-defined particle trajectory. In the case of this analysis, we only deal with the two classes of tracks that are most likely to be true particles. The ideal situation, DC quality 63, requires a unique UV hit in the drift chamber, use both X wires, and is further matched to a unique PC1 hit. The second best option, DC quality 31, matches all of the previous requirements, but has an ambiguous match to a PC1 hit.

While a given track projection will pass very near all of the hits associated with that track, it is not expected that there should be perfect agreement between the track and an individual hit. The difference between a given track projection and its associated hit is calculated and recorded, and referred to as the tracking residual, it is given as displacements along $\phi$ or z. For a given detector the collection of all tracking residuals along $\phi$ or z will form a gaussian distribution. This distribution is scaled so that the gaussian width parameter, $\sigma$, is normalized to one and an analyzer may choose to select only tracks which fall within a certain numerical constraint. This selection is referred to as a track matching cut. For this analysis we have selected tracks that fall within +/- $3\sigma$ of the mean in both $\phi$ and z for the PC3 and again in the TOF-W when using it for particle identification. The scaled tracking variables are renamed sdz, sd$\phi$, to differentiate from the raw residual variables, dz and d$\phi$.

Including those selections mentioned above, all tracks are subjected to the follow-

ing set of cuts to assure good track quality:

| Cut | Details |
|---|---|
| DC Quality | DC Quality = 31 or 63 |
| DC Acceptance | $3 <$ \|Drift Chamber Z\| $< 70$ |
| PC3 Tracking | PC3 \|sd$\phi$\| $< 3.0$ and PC3 \|sdz\| $< 3.0$ |
| General Tracking | $p_T > 300$ MeV/c |
| Detector Acceptance | DC, PC1, and PC3 fiducial maps |
| Arm Selection | Track in the West Arm |

Table 2: Track-Level Applied Cuts

Tracks are also checked in pairs for the DC "ghost cut," a phase-space cut on the DC spatial variables. Under certain circumstances, the DC wires may produce ambiguous tracking information, creating an artifact track that mirrors a true track. For the circumstances in which this may occur, we cut both tracks to avoid contamination. For track pairs, we cut tracks that are within 0.07 radians of each other in DC$\phi$ and that are within 0.5 cm of each other in DCz, where DC$\phi$ and DCz are the reconstructed hit locations for $\phi$ and z within the Drift Chambers. For more information on this cut, see AN328 [33]. The DC acceptance cut listed in Table 2 avoids the DC support structure and is supplemental to the fiducial map, described later.

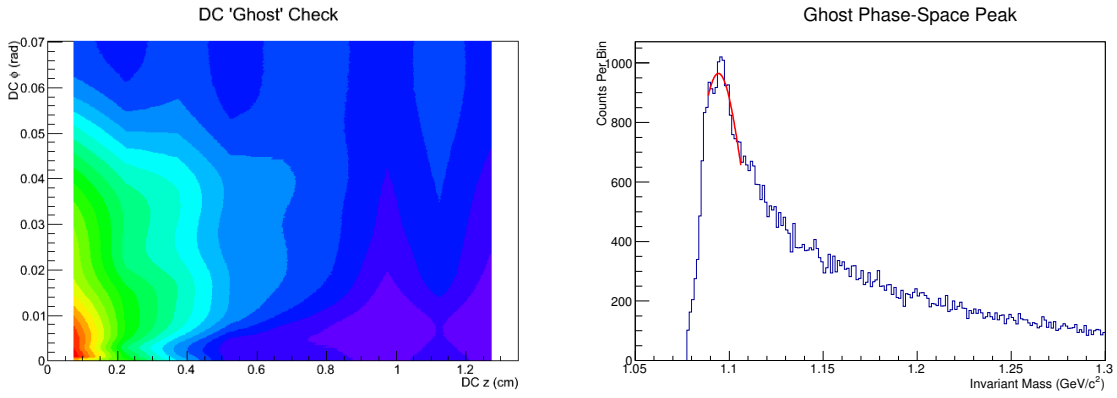


Figure 20: Drift Chamber *ghost* selection
Delta DC$\phi$ plotted against delta DCz of the two particles, we cut 0-0.5 cm in DCz and 0-0.07 rad in DC$\phi$. On the right, the mass distribution when requiring the phase region to be inside the ghost cut region; the mean for the fit shown is 1.094 GeV/c$^2$.

For tracks that are identified in the TOF-W we add the following requirements:

| Cut | Details |
|---|---|
| TOF-W Quality | TOF-W good strip selection |
| TOF-W ADC | $60 < \frac{adc_{up}+adc_{down}}{2} < 600$ |
| TOF-W Tracking | TOF-W $\|\text{sd}\phi\| < 3.0$ and $\|\text{sdz}\| < 3.0$ |
| Proton Identification | $3\sigma$ normalized 'isProton' TOF-W $m^2$ to ID proton |

Table 3: Additional PID Method Cuts

The *isProton* cut is based on Gaussian fits to the proton mass peak as seen in the TOF-W $m^2$.

### 3.3 Analysis Method

In order to extract lambda yields we use particles in a single event to generate an invariant mass spectrum based on our particle choices: In the no-PID method this means two tracks within a single arm with opposite sign charge. The positive track is assigned the proton momentum in the invariant mass calculation, while the negative track is assigned a pion mass. When repeating the process for the anti-lambda baryon, every aspect of the analysis remains the same, save for the charge; the positive track is assigned the pion mass, while the negative track is assumed to be an anti-proton. For the TOF-W PID method the procedure is similar, with the addition that the proton is now specifically identified in the TOF-W from the $m^2$ distribution. Using the TOF-W, a particle's mass is found by $m^2 = p^2[\frac{t^2c^2}{pl^2} - 1]$, where p is the track momentum, t is the elapsed time from initial collision to detection, pl is the reconstructed path-lenth from collision to detector, and c is the usual speed of light.

The invariant mass plot contains the lambda peak itself, as well as a large background from the combinations of all particles in the event that are not from lambdas themselves. This background shape is estimated using a mixed event method where pion candidates are stored in a buffer and then mixed with all current event proton candidates. When mixing, the buffered pions are selected so that they match the current event closely in centrality (10%) and the z vertex (10 cm) of the event collision

as determined by the BBC. Track pairs belonging to the phase-space in DC$\phi$ and DCz within the ghost-cut described above are similarly not selected when building the mixed events shape. For each final data point we wish to show, the mixed event is normalized to the single-event invariant mass plot with a constant fit outside the lambda mass range; in our case, from 1.123 to 1.160 GeV/c$^2$. Any single-event correlations, such as the lambda, are not represented in the mixed event, so scaling the mixed event shape and subtracting it from the single-event invariant mass, one is left with primarily lambdas. We can then fit this subtracted yield in order to extract the lambda signal for each $p_T$ bin.

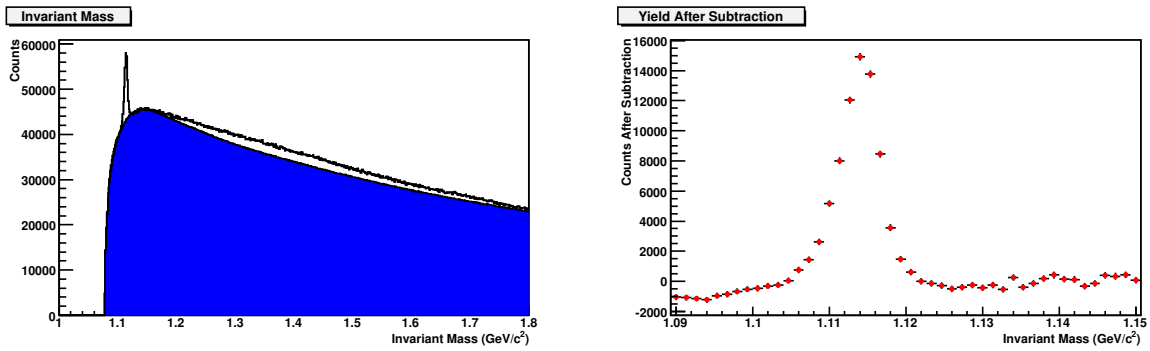


Figure 21: Lambda invariant mass plot for the no-PID method.
(Left) The mixed event shape is in blue and normalized to the single-event plot outside the lambda mass window. The differences are from single-event correlations, such as a $\phi \to K^+ + K^-$ decay that is assigned proton and pion masses for the kaons in the invariant mass calculation. The plot on the right shows the peak shape after subtraction.

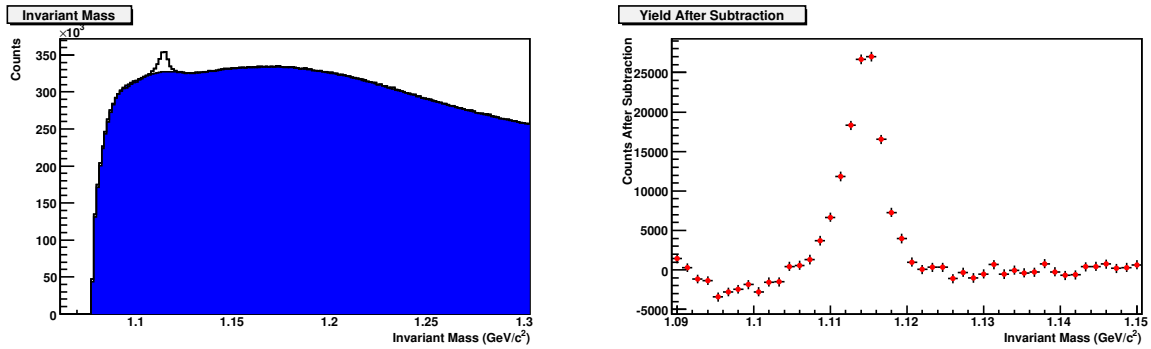


Figure 22: Example of the lambda shape for the TOF-W PID method in a 0-20% centrality class.

After we have the subtracted yield invariant mass shape, we fit the lambda peak using a double-gaussian plus a background function $F_{background}$, shown below.

$$F_{background} = a + \frac{b}{x} + \frac{c}{x^2} + \frac{d}{x^3} + \frac{e}{x^4} \tag{4}$$

In general, the range of the fit is from 1.098 to 1.140 GeV/c$^2$ in invariant mass, but for the few cases where the fit-function itself does not easily converge to a good fit in this window, the fit window may be changed slightly. The lambda yield is taken from the integration of the double-Gaussian component of our fit in a range +3$\sigma$ and -5$\sigma$ about the Gaussian mean, to cover the peak and the low-mass tail. After initial fits, the $p_T$ trend for the width of the primary peak is fit with a simple polynomial. For a second pass of fits, limitations are placed on the width of the main peak gaussian, +/- 30% of the peak $\sigma$ as defined by the previous fit, in order to encourage the fitting routine to converge properly. Examples of background-subtracted peaks with fit functions can be seen in Figs.23-30.

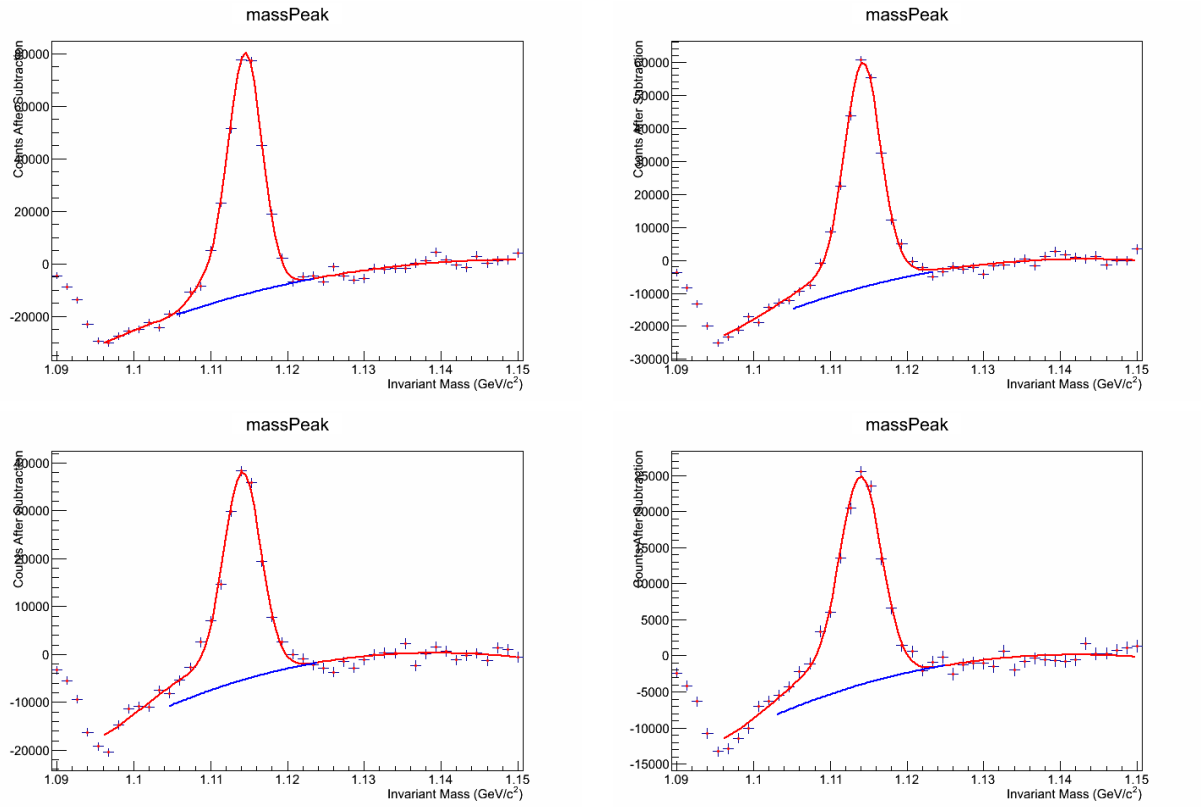


Figure 23: No-PID, 0-20% centrality, peaks in 200 MeV/c $p_T$ bins 2.0 to 2.8 GeV/c

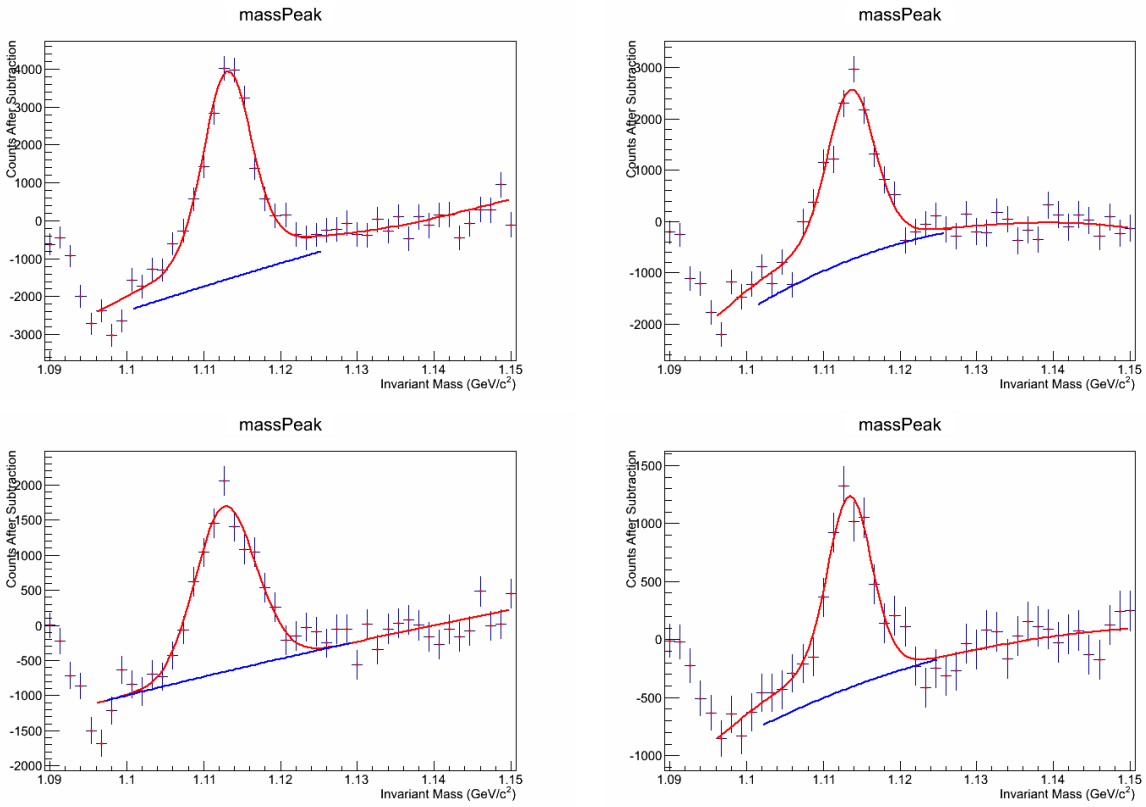


Figure 24: No-PID, 0-20% centrality, peaks in 200 MeV/c $p_T$ bins 3.4 to 4.0 GeV/c

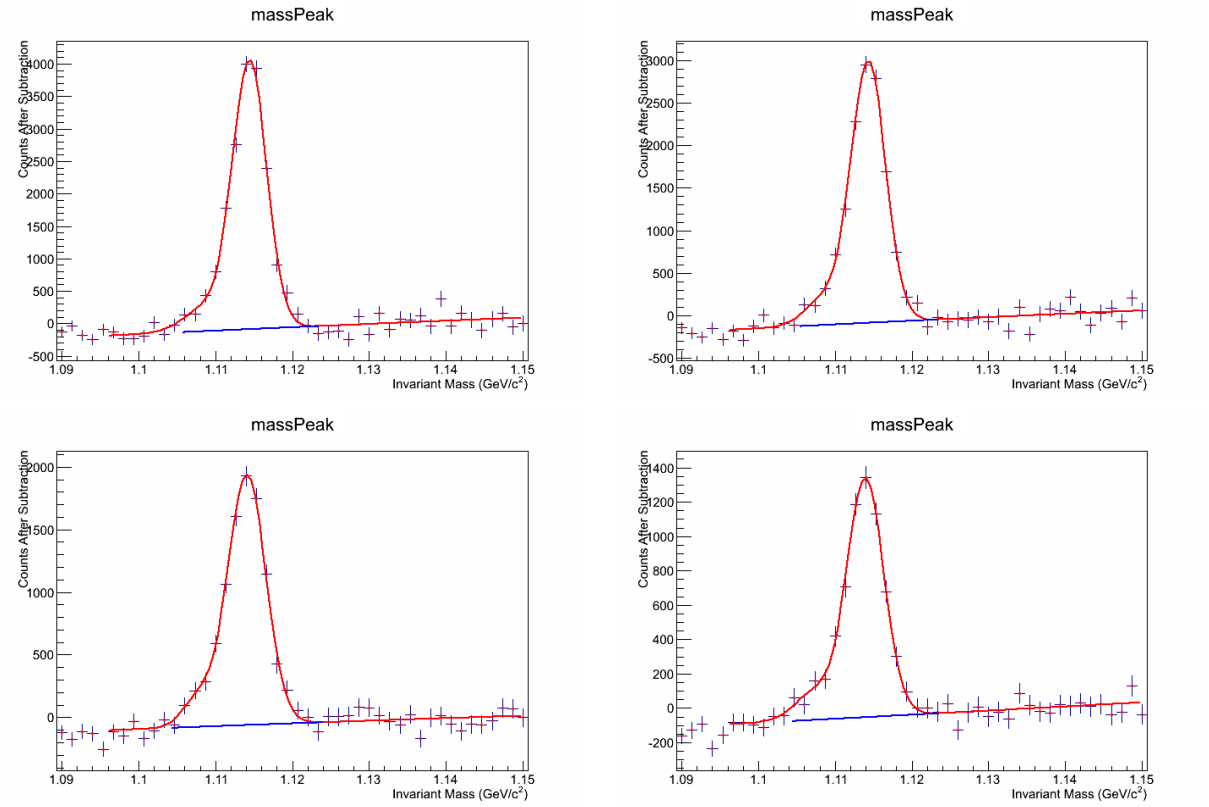


Figure 25: No-PID, 60-92% centrality, peaks in 200 MeV/c $p_T$ bins 2.0 to 2.8 GeV/c

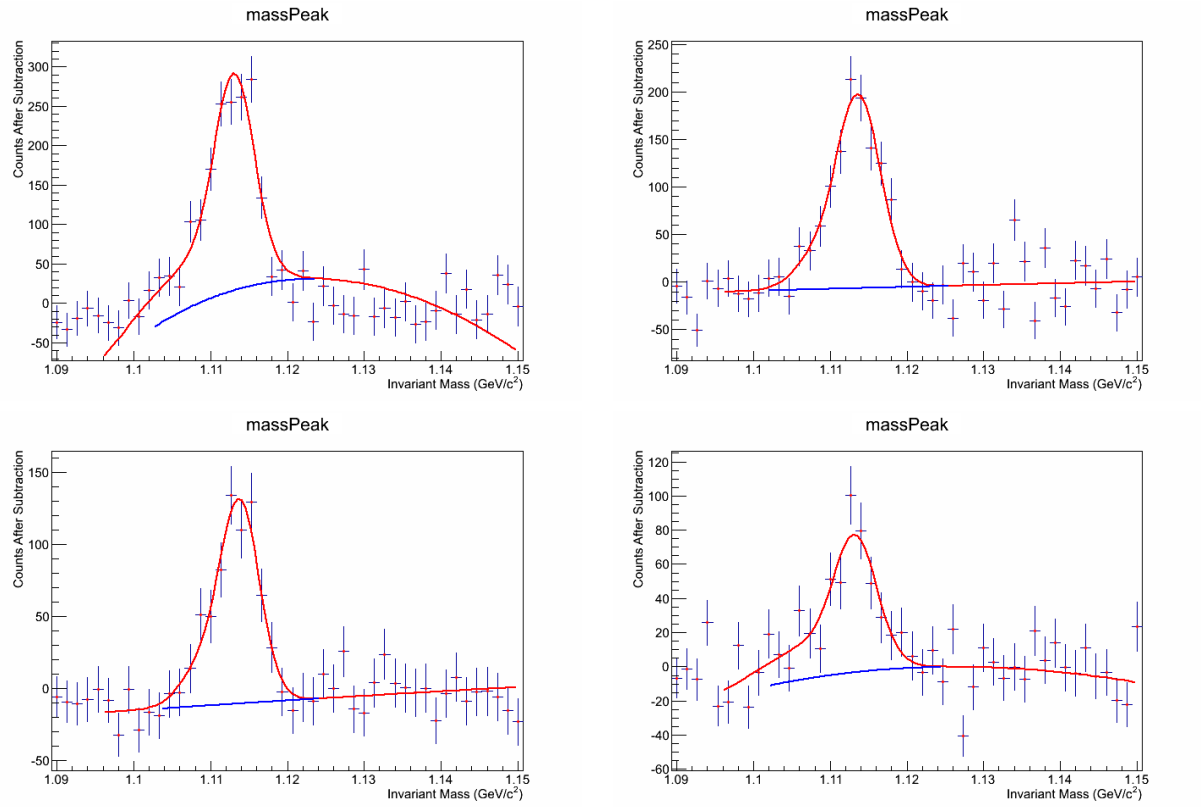


Figure 26: No-PID, 60-92% centrality, peaks in 200 MeV/c $p_T$ bins 3.4 to 4.0 GeV/c

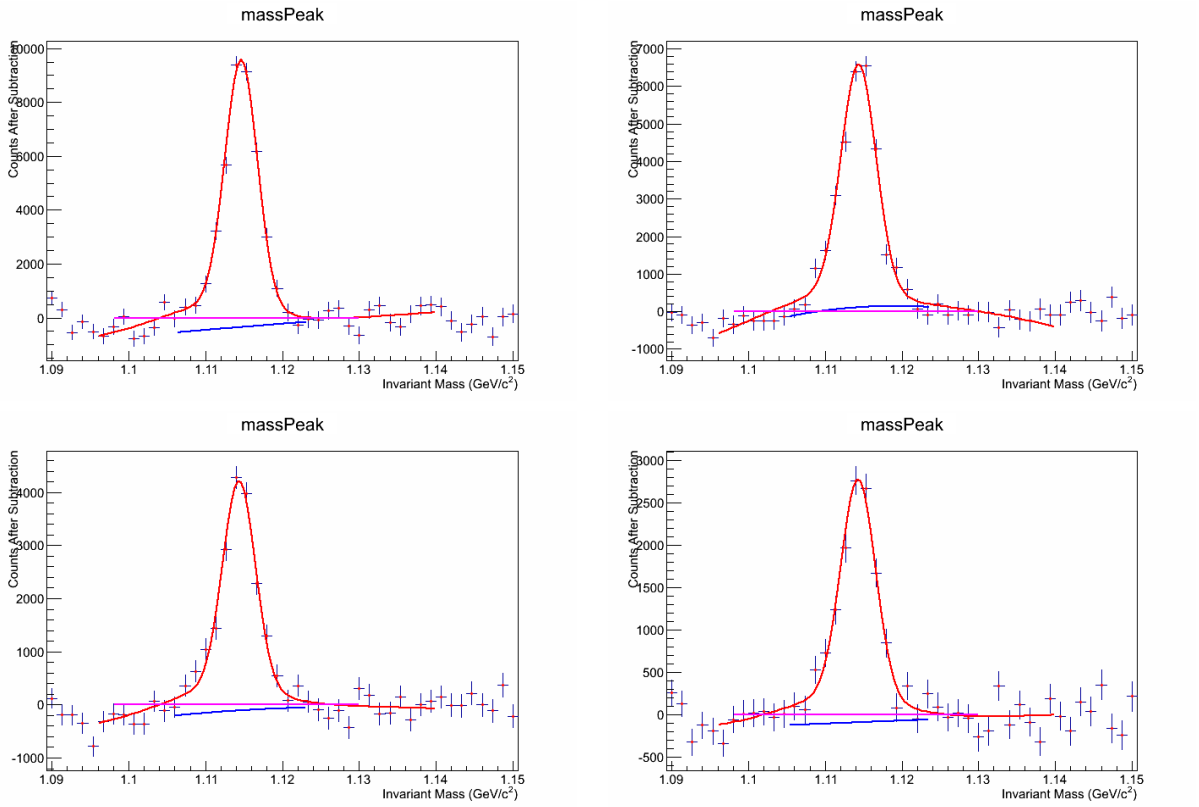


Figure 27: PID, 0-20% centrality, peaks in 200 MeV/c $p_T$ bins 2.0 to 2.8 GeV/c

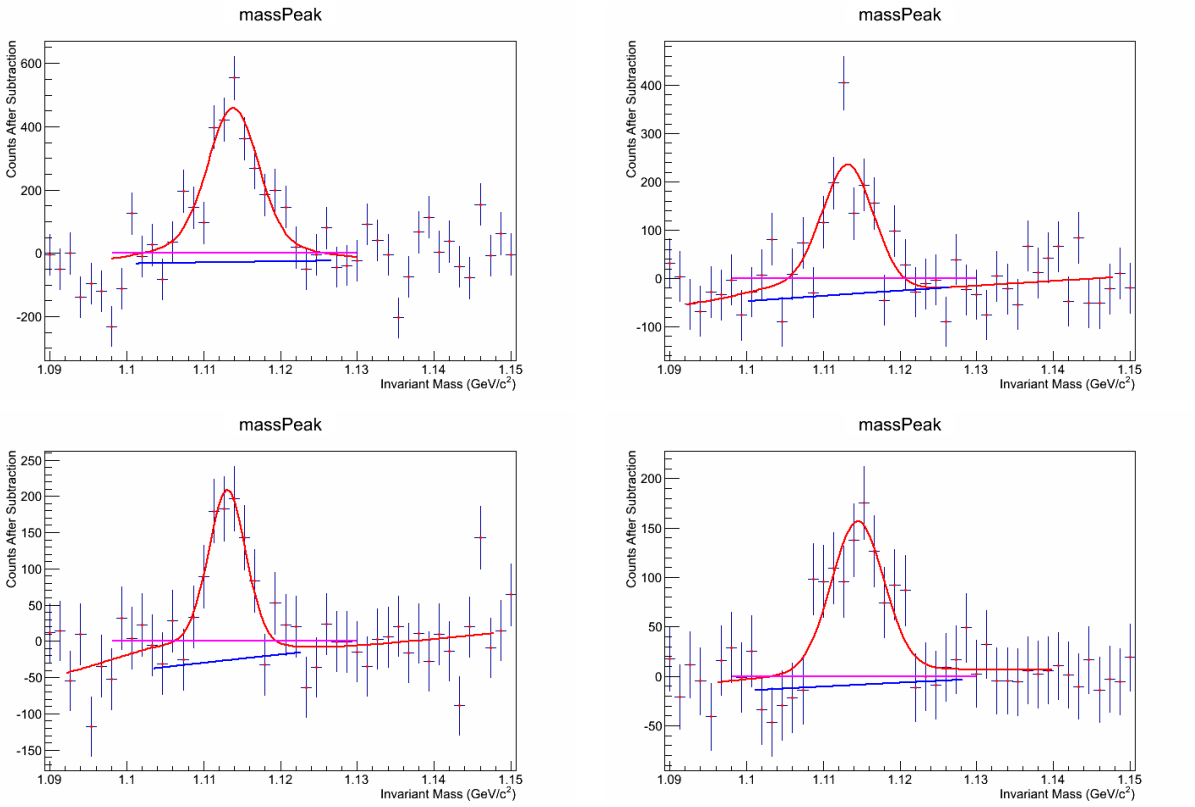


Figure 28: PID, 0-20% centrality, peaks in 200 MeV/c $p_T$ bins 3.4 to 4.0 GeV/c

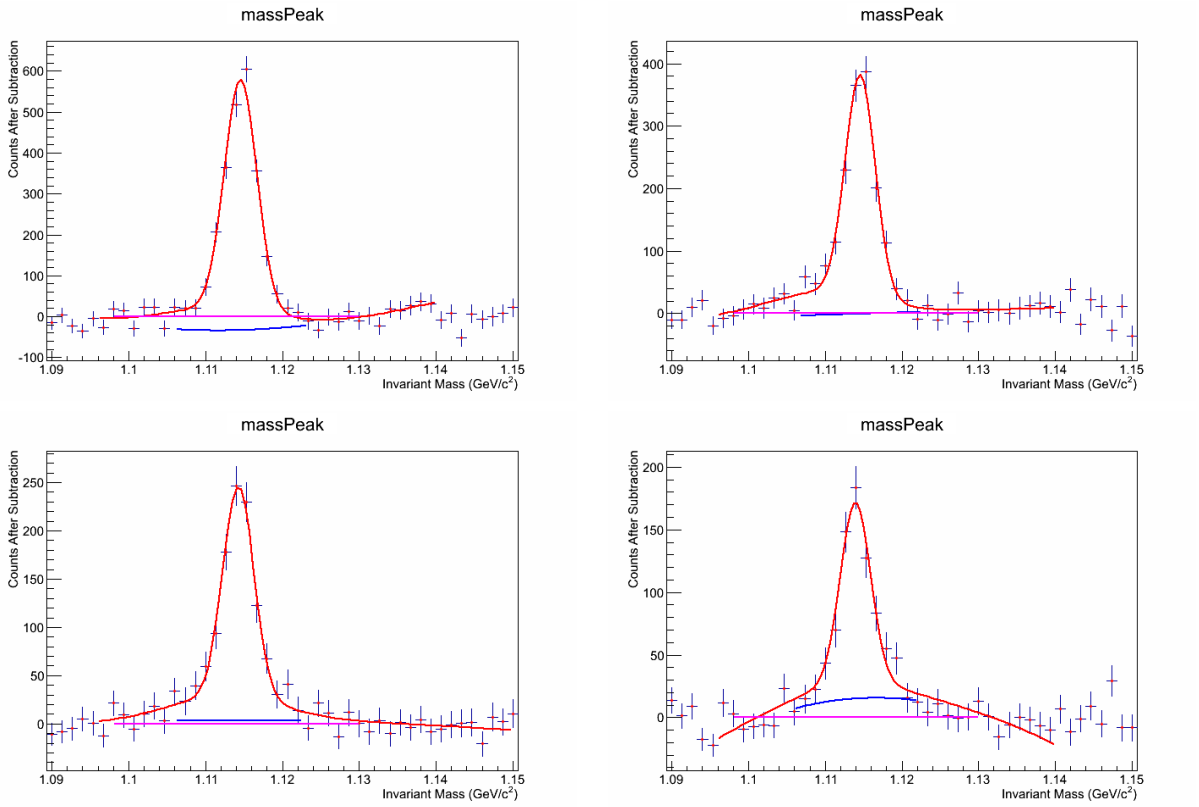


Figure 29: PID, 60-92% centrality, peaks in 200 MeV/c $p_T$ bins 2.0 to 2.8 GeV/c

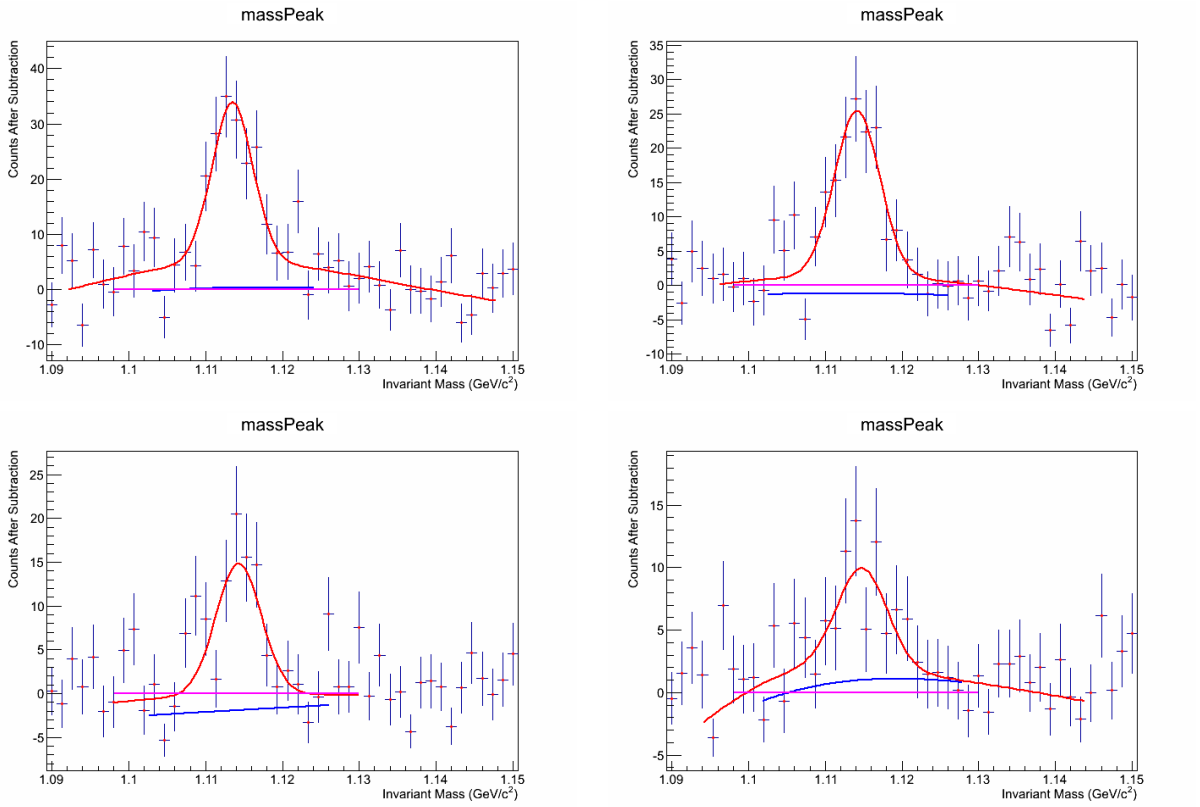


Figure 30: PID, 60-92% centrality, peaks in 200 MeV/c $p_T$ bins 3.4 to 4.0 GeV/c

### 3.4 Corrections and Systematic Uncertainties

The procedure described above generates a raw lambda spectrum based on what is collected by the detectors, but lacks information regarding detector efficiencies, acceptances, and other effects that will change the physics messages of our final plots. In order to correct for these effects we turn to simulations. We generated 20M single lambda events for the +− field configuration, as well as 20M −+ events and ran them each through analysis code identical to that used in our real data analysis, now adapted to run over simulated data. The simulated particles are generated using the EXODUS event generator with the following requirements:

1. Flat distribution of the lambda $p_T$ from 0-10 GeV/c.
2. Flat rapidity distribution within +/− 0.6.

3. Flat azimuthal coverage, $\phi = 0 - 2\pi$.

4. Flat $z_{vertex}$ distribution within +/− 30cm.

The lambdas are then fed into PISA, an internal PHENIX software package that models the detectors, handles the particle decay and detector response characteristics. Because of the decay-in-flight characteristics of the lambda daughters, correcting simulated detector tracking residuals with these is incorrect. Instead, we used the residual corrections based on the single particle Run7 analysis AN814 [34] and add our own corrections based on a sample of single pion simulations. After these corrections we find the agreement between tracking residuals in real data and those in our simulations to be adequate. It is not required that simulation and real data match perfectly in this regard; because we select tracks based on +/- 3$\sigma$ track-matching, a discrepancy between real data and simulation of 0.1 in the residual width equates to a change in extracted yield of 0.077% and a deviation of 0.05 in the residual mean results in change of 0.013%. The real data tracking residuals are handled by existing calibrations and are adequate for use; we present the tracking residuals from simulation in Figs.31-38, which have been calibrated by our own analysis.

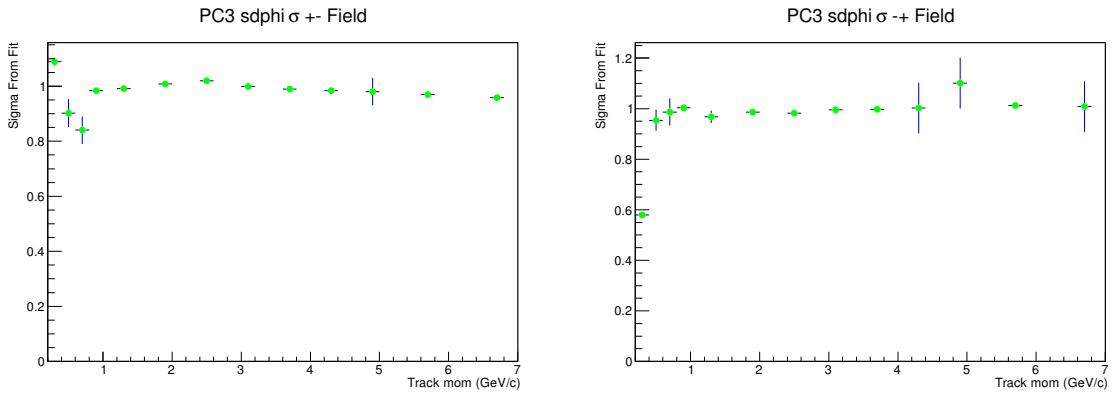


Figure 31: Normalized PC3 tracking residual sdphi width $\sigma$ in single pion simulations (+- left, -+ right)

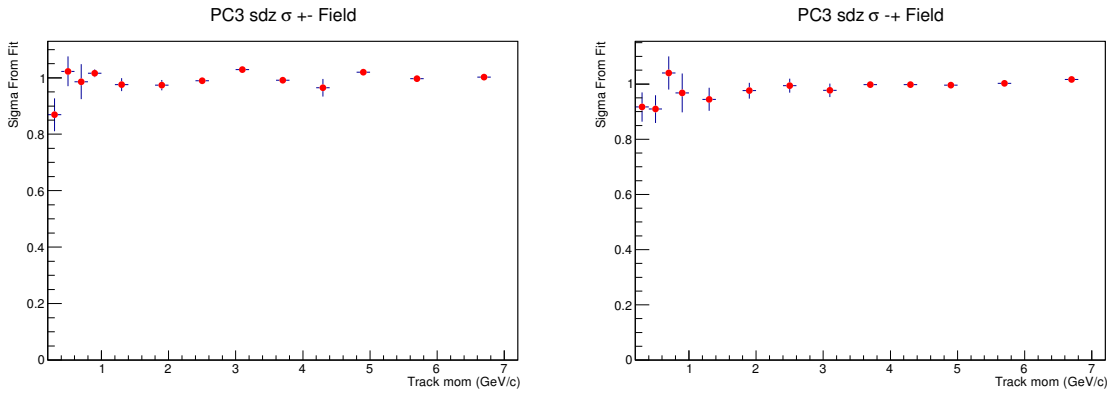


Figure 32: Normalized PC3 tracking residual sdz width $\sigma$ in single pion simulations (+- left, -+ right)

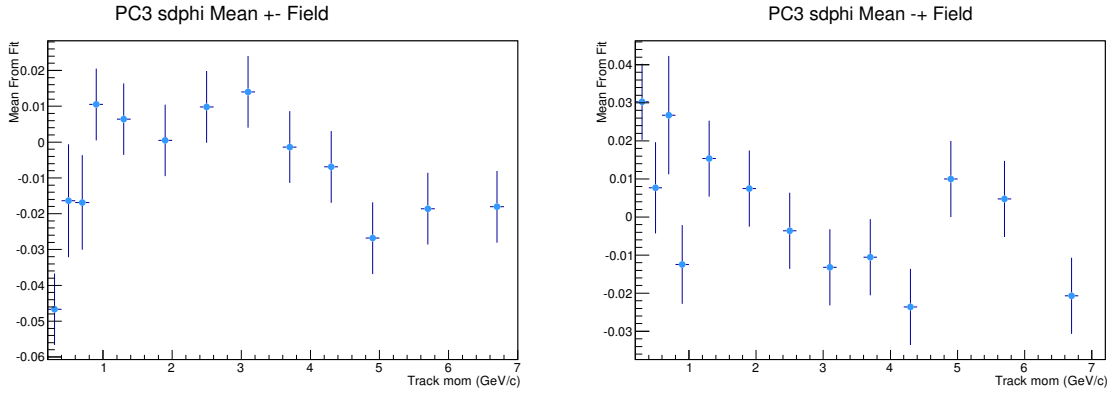


Figure 33: Normalized PC3 tracking residual sdphi mean in single pion simulations (+- left, -+ right)

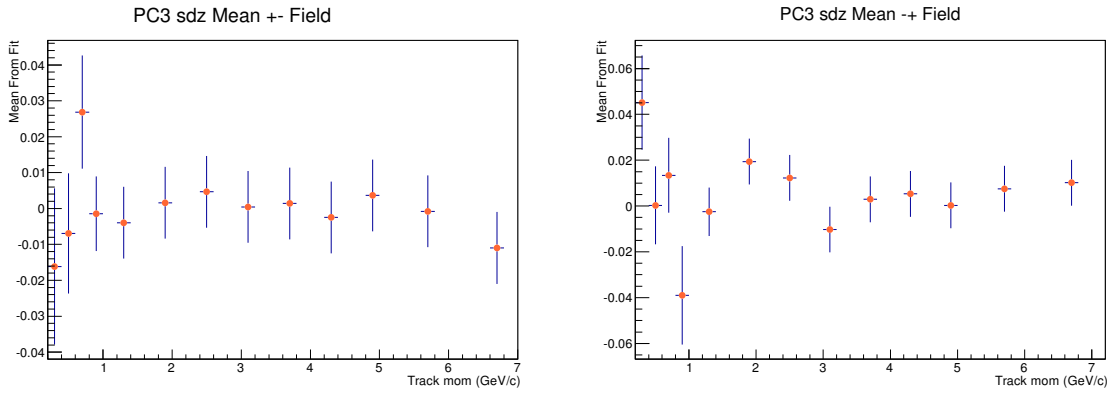


Figure 34: Normalized PC3 tracking residual sdz mean in single pion simulations (+- left, -+ right)

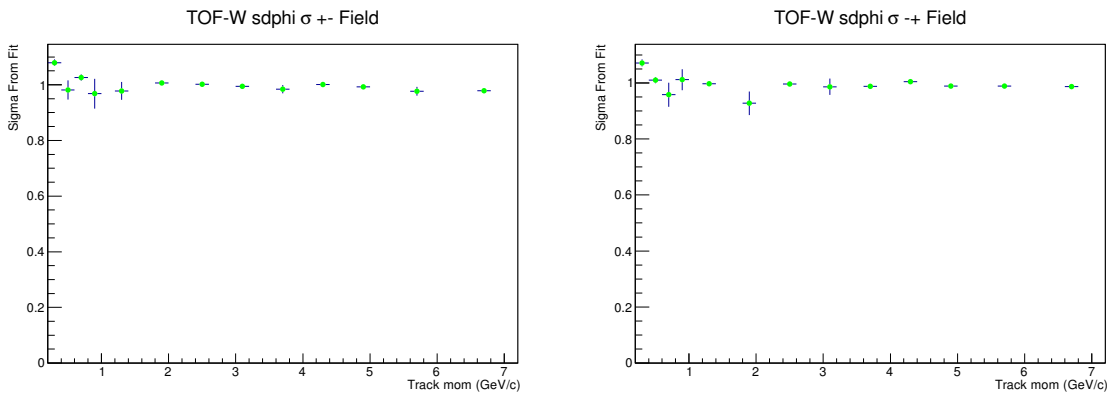


Figure 35: Normalized TOF-W tracking residual sdphi width $\sigma$ in single pion simulations (+- left, -+ right)

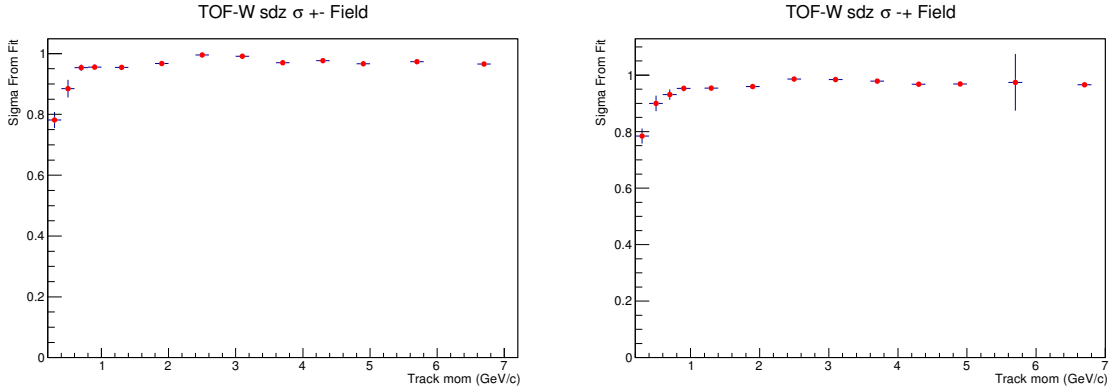


Figure 36: Normalized TOF-W tracking residual sdz width $\sigma$ in single pion simulations (+- left, -+ right)

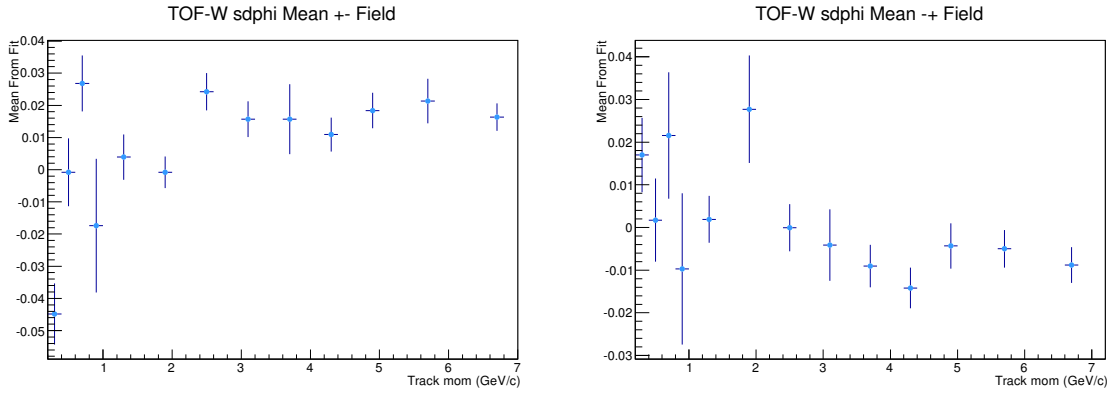


Figure 37: Normalized TOF-W tracking residual sdphi mean in single pion simulations (+- left, -+ right)

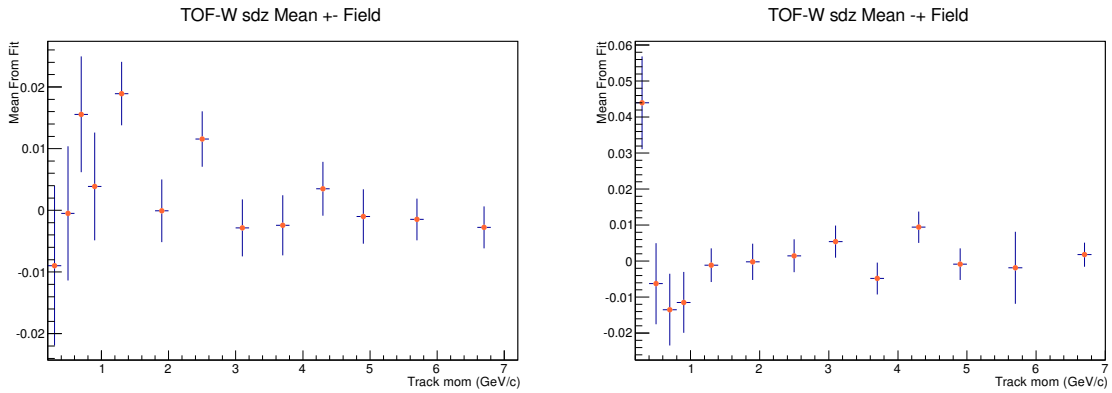


Figure 38: Normalized TOF-W tracking residual sdz mean in single pion simulations (+- left, -+ right)

In addition to ensuring that the tracking in the PC3 and TOF-W match between simulated and real data, it is very important to also be certain that the fiducial acceptance of each detector behaves consistently when comparing the real and simulated data sets. Over time, small parts of the detectors may function outside of their intended efficiencies. Detectors are designed to be robust, but damage due to environmental wear, radiation, voltage supply irregularities, etc., may impact a detector element's ability to produce a clean signal. In order to demand that detectors exhibit the same live and dead areas, we produce maps from each detector using basic hit information in a given detector and artificially introduce a set of cuts over each detector such that any discrepancy in detector geometry or efficiency is ignored in both real and simulated data. The resulting fiducial maps are applied equally to both real and simulated data. It is worth noting that while the maps shown in Figs.39-42 typically mask low efficiency areas, there are also elements that float electronically high and saturate their signals, these are usually masked away in the data at an earlier stage of data processing.

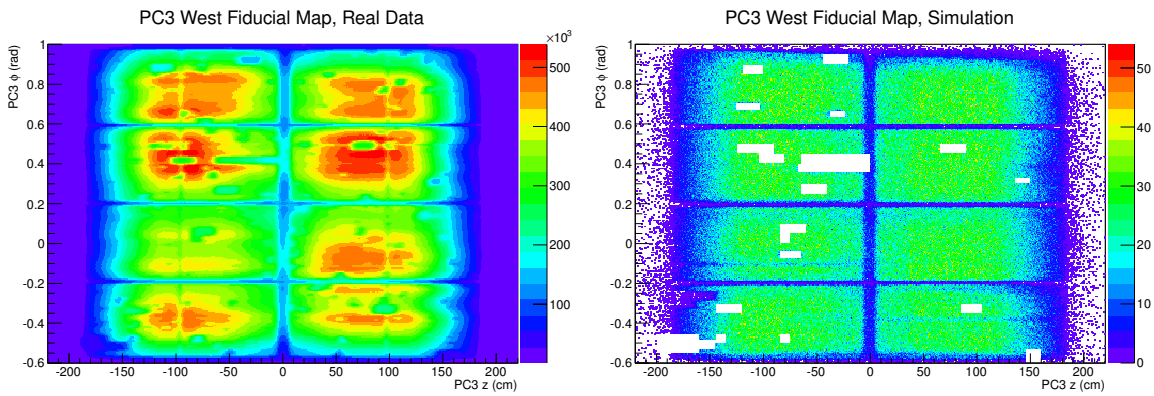


Figure 39: PC3 acceptance in the west arm in real data (Run7 +- left) before fiducial map and in simulation after cuts (+- $\Lambda$ right).
The occupancy in each plot should not neccessarily be expected to match perfectly, rather that any major defect be masked away in either data set.

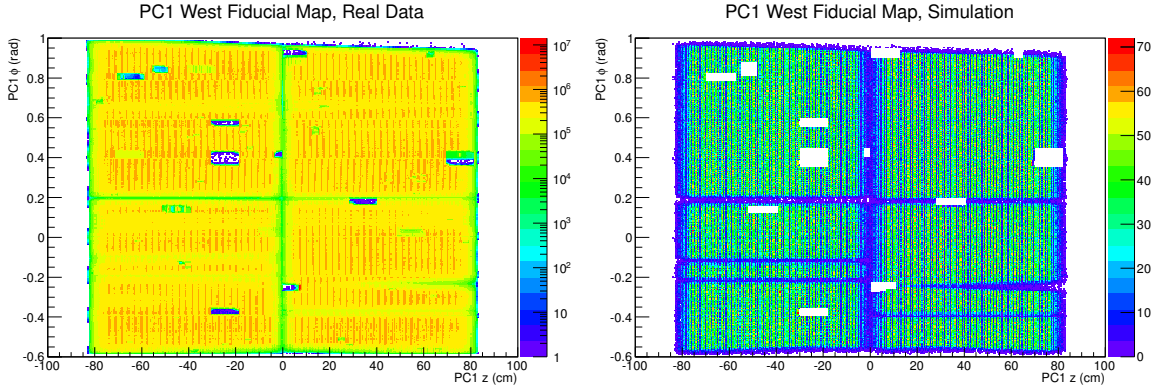


Figure 40: PC1 acceptance in the west arm in real data (Run7 +- left) before fiducial map and in simulation after cuts (+- $\Lambda$ right).
Again, the occupancy in each plot should not neccessarily be expected to match perfectly, rather that any major defect be masked away in either data set.

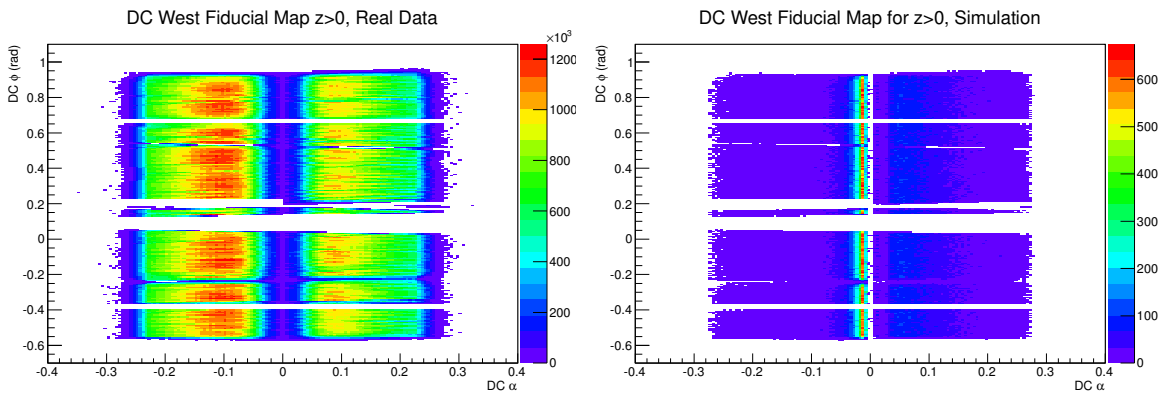


Figure 41: DC (positive z) acceptance in the west arm with fiducial map applied in real data (Run7 +- left) and in simulation (+- Λ right).
Again, the occupancy in each plot should not neccessarily be expected to match perfectly, rather that any major defect be masked away in either data set.

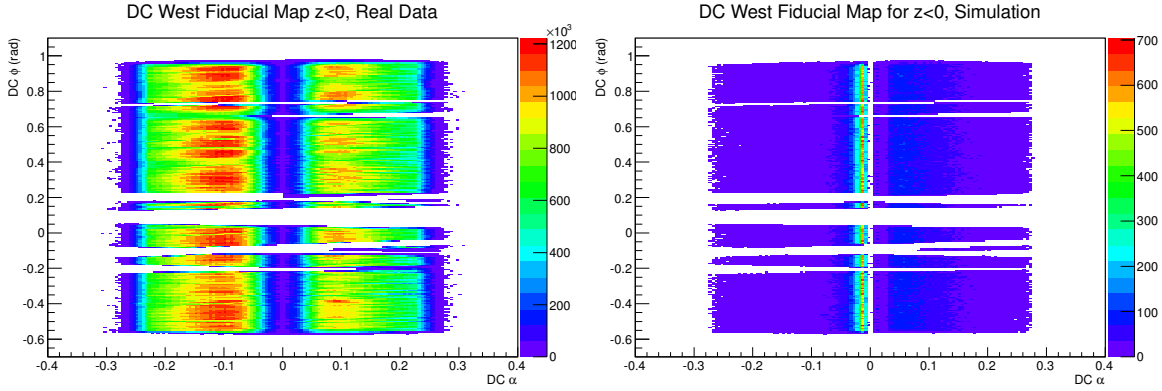


Figure 42: DC (negative z) acceptance in the west arm with fiducial map applied in real data (Run7 +- left) and in simulation (+- Λ right).
Again, the occupancy in each plot should not neccessarily be expected to match perfectly, rather that any major defect be masked away in either data set.

After all data consistency concerns are addressed in the comparison between real data and simulation, it is also important to verify that the reconstructed kinematic behavior of our particles are also in agreement. We find that the simulation and the data match reasonably well, though the width of the real data peaks is somewhat greater than the corresponding simulation peak. We have plotted the evolution of the fitted mean in Fig.44 as well as the standard deviation in Fig.43.

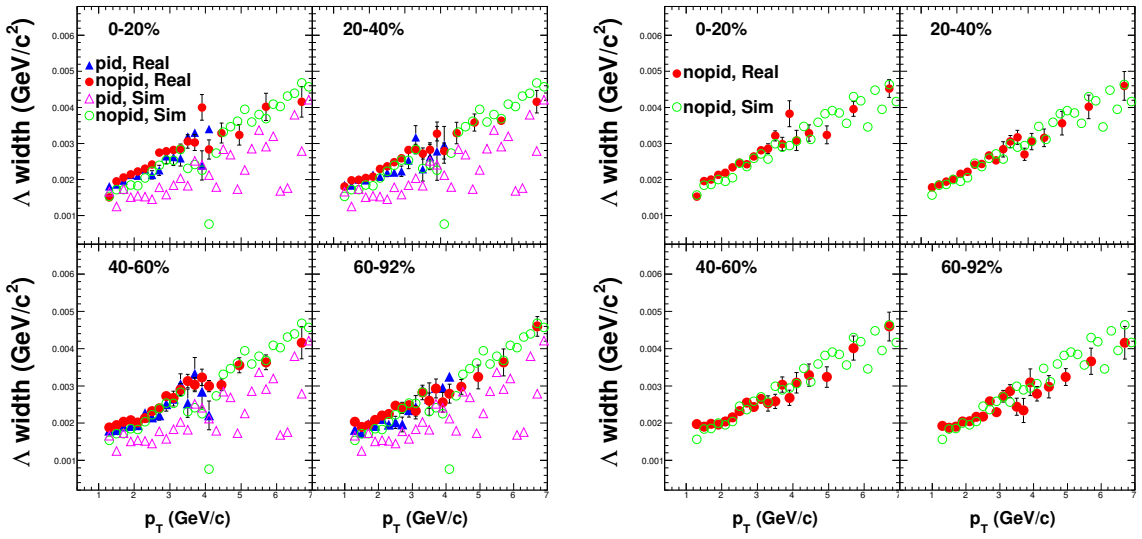


Figure 43: Gaussian peak width $\sigma$ from real data compared to simulations
+− field configuration is on the left, −+ field on the right.

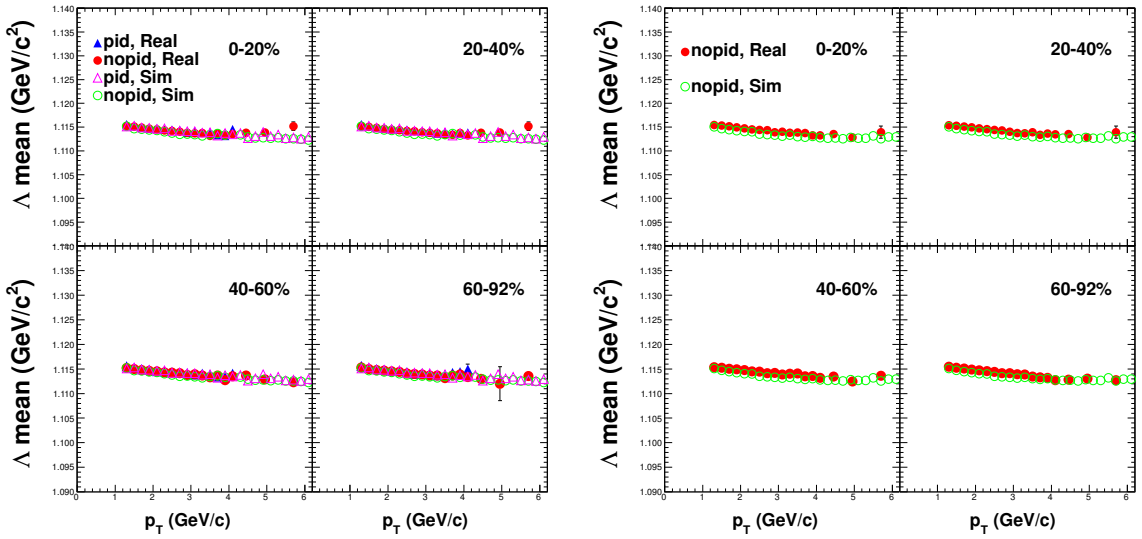


Figure 44: Evolution of the gaussian mean
Real data (solid shapes) vs simulation (open shapes); very little difference is seen.
+− field configuration is on the left, −+ field on the right.

By reconstructing and counting the single lambdas and comparing the resulting sum to the number of lambdas originally generated in each bin we derive a correction factor (CF). This correction factor simultaneously accounts for detector efficiencies and acceptance effects, and is scaled to account for the fact that we throw particles

in 1.2 $\eta$, but normalize to 1.0 $\eta$. For our study we fit the trend and use the fit when correcting our data, as opposed to point by point. We have plotted this factor, by method, in Fig.45.

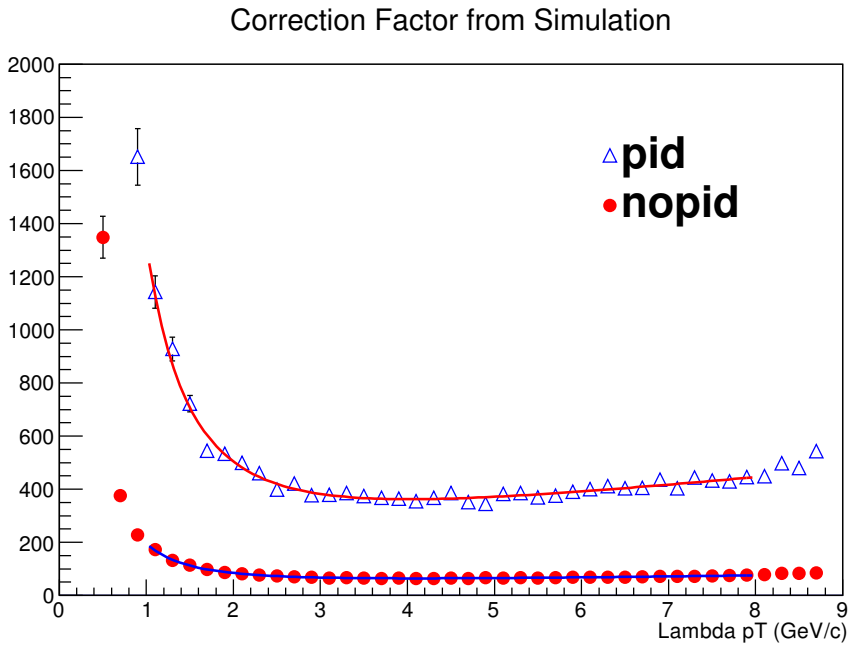


Figure 45: Correction factors from single $\Lambda$ particle simulations
The steep rise at low $p_T$ is due to detector acceptance and our 0.3 GeV/c cutoff for accepted tracks.

Because the single-lambda simulations cannot correct for detector effects that are seen at high multiplicity, such as high detector occupancy effects, we also utilize PHENIX embedding software. In this procedure simulated single lambdas are inserted in real data events and passed through PISA, making certain that the original vertex is maintained for each event. The efficiency with which the lambdas are recovered in real data compared to their recovery without the surrounding event tells us about the losses we expect to occur in real data for each centrality class we have defined. These efficiency curves are plotted in Fig.46. The study was done for both field configurations and less than a 1% difference was seen for each point. The embedding efficiency goes together with the correction factor and the lambda branching ratio to

the $p+\pi^-$ channel (63.9% as measured by PDG) to give us a corrected yield. In order to finally obtain the invariant yield from the raw spectra extraction we multiply the raw yield by the following:

$$Y_{invariant} = Y_{raw}\,\frac{CorrectionFactor}{0.639\,\epsilon_{embed}}\,\frac{1}{2\pi p_T}\,\frac{1}{N_{events}\,binwidth_{p_T}\,binwidth_{centrality}} \qquad (5)$$

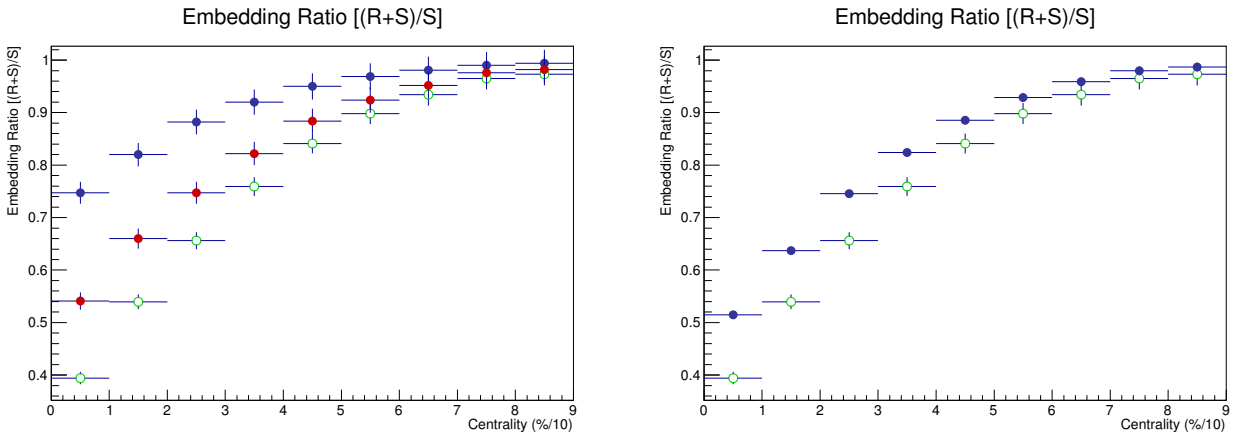


Figure 46: Pion, proton and lambda embedding ratios, from top to bottom (left) and lambda embedding ratio for noPID and PID methods, top to bottom (right).
In both cases, $\epsilon_p\epsilon_\pi = \epsilon_\Lambda$. All points are $p_T$ averages over 0-9 GeV/c.

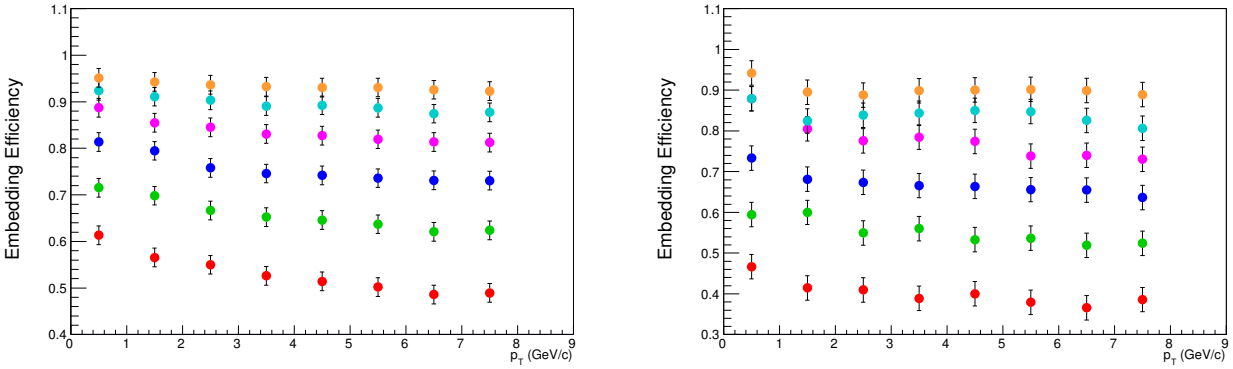


Figure 47: $P_T$ dependence of embedding ratio for No-PID (left), and TOF-W PID (right).
In each, the trends represent 10% centrality bins starting from 0-10% at the bottom and running through 50-60% at the top. Each trend is fit by a $A + B\,x + \frac{C}{x}$ formula and the data is scaled by the fit.

Given a perfect detector with no resolution limitations a simulation thrown with a flat-$p_T$ distribution would be adequate to describe the correction factors we wish to derive from it. However, the reality of the PHENIX experiment with respect to lambda baryons is quite different. As the lambdas travel further away from the reconstructed vertex before decay, the PHENIX tracking routines begin to misreconstruct aspects of the daughter particles, such as momentum, mass, or charge, resulting in significant smearing along the reconstructed $p_T$-axis. Because of this, the abundance of observed lambda baryons at a given $p_T$ is directly related to the relative abundances of lambdas in nearby $p_T$ regions, which are misreconstructed and counted at the wrong point along the $p_T$-axis. In order to properly match the effects occurring in real data, our simulation must be artificially weighted in an attempt to match the spectrum of produced lambda baryons. Since that spectrum is precisely what we are attempting to measure in this study, we instead fit the spectrum of a well-measured particle that is expected to have a similar distribution, in this case the proton. The proton specta from Ref. [35] is fit using the function $f_{tsallis}(p_T) = \frac{1}{2\pi}\frac{dN}{dy}\frac{(n-1)(n-2)}{nT(nT+m_0(n-2))}\left[1+\frac{m_T-m_0}{nT}\right]^{-n}$, where $m_T = \sqrt{p_T^2+m_0^2}$, shown in Fig.48, and we replace the proton rest mass with that of the lambda baryon in the function. This provides a starting point for simulation weighting, which we then use to produce a lambda spectrum from real data and iterate the process, with the assumption that the process converges toward the real distribution.

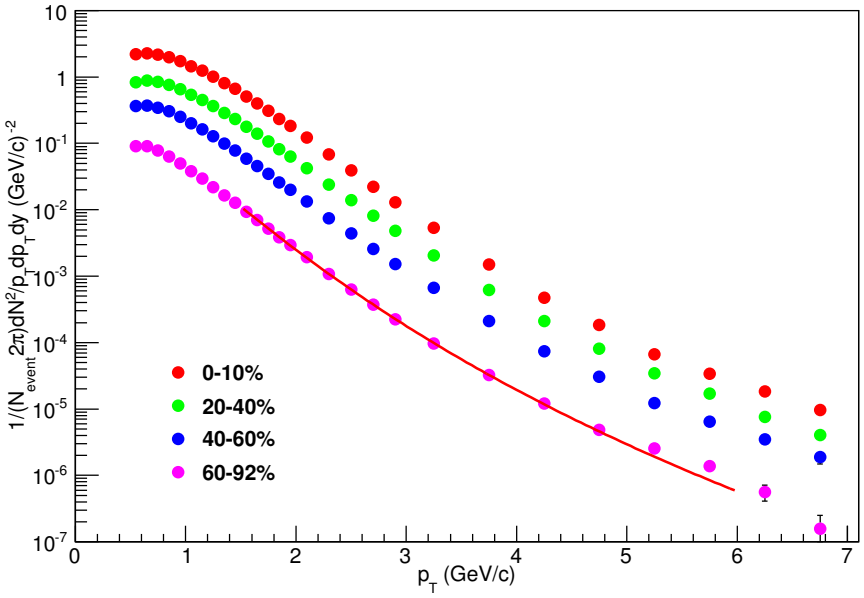


Figure 48: Proton spectra fit with the function $f_{tsallis}(p_T)$
Resulting values give n = 13.45, T = 0.227, and $\frac{dN}{dy} = 0.0799$

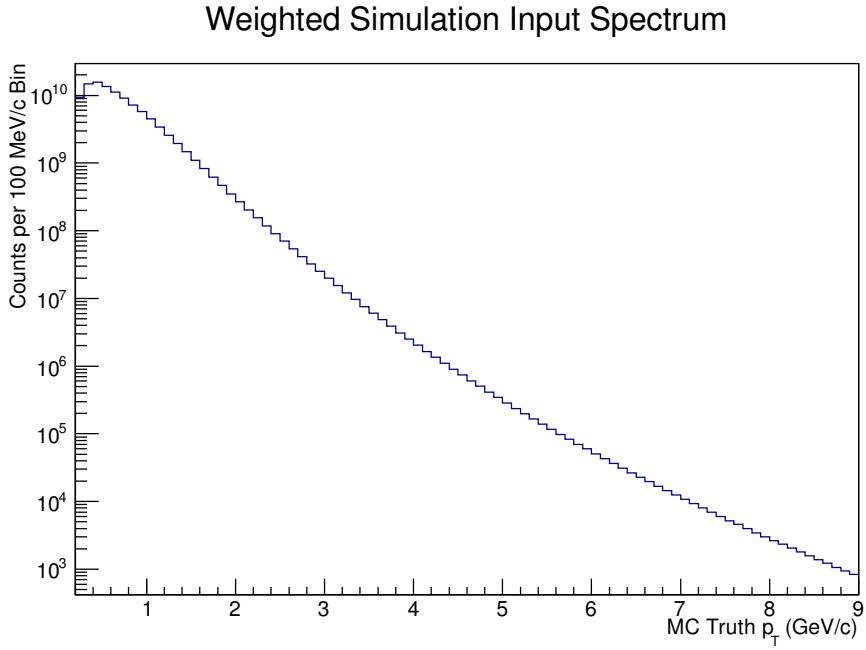


Figure 49: Lambda simulation input spectrum, weighted by modified proton-fit results.

After the simulation has been properly weighted, reconstructed lambda peaks in

real data and simulation behave consistenly, including the low-mass tail associated with decay-in-flight momentum misreconstruction, as seen in Fig.50 and Fig.51.

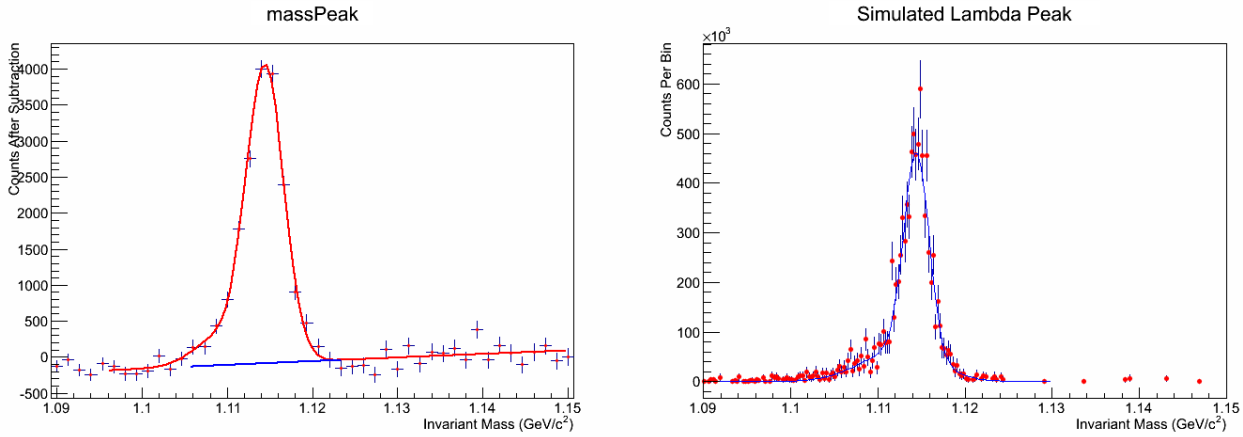


Figure 50: Simulation vs real data peaks for a $p_T$ window of 2.0-2.2 GeV/c
Low-mass tails behave similarly, which is not the case before simulation weighting.

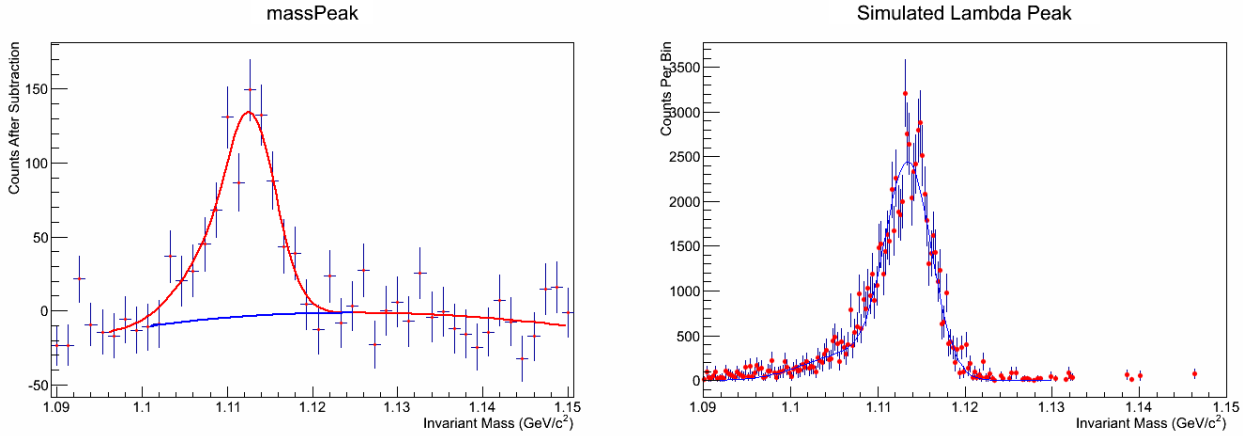


Figure 51: Lambda mass peak as seen in real data (left) and singles simulation (right) for 4.0-4.2 GeV/c in reconstructed lambda $p_T$.

Beyond the statistical uncertainty for each data point, a systematic uncdertainty must be computed and is related to our hardware and our analysis method. For systematic uncertainties we consider the following:

| Systematic | Method of Evaluation |
|---|---|
| Background Function | Vary background fit (4); compare to $(A + \frac{B}{x} + \frac{C}{x^2})$ |
| Fitting Fidelity | Fit range modified +/− 10% |
| Magnetic Field | Repeat analysis entirely in two sets of data |
| Tracking Fidelity | Alter tracking requirements in simulation and real data |
| Embedding Systematic | Based on previous PHENIX estimates |
| Unfolding Systematic | Vary unfolding parameters, vary input matrix |

Table 4: Systematic uncertainty checks

In Fig.52 we plot the ratio of our extracted yield before and after a change of the background fit function. The associated systematic uncertainty is 2%.

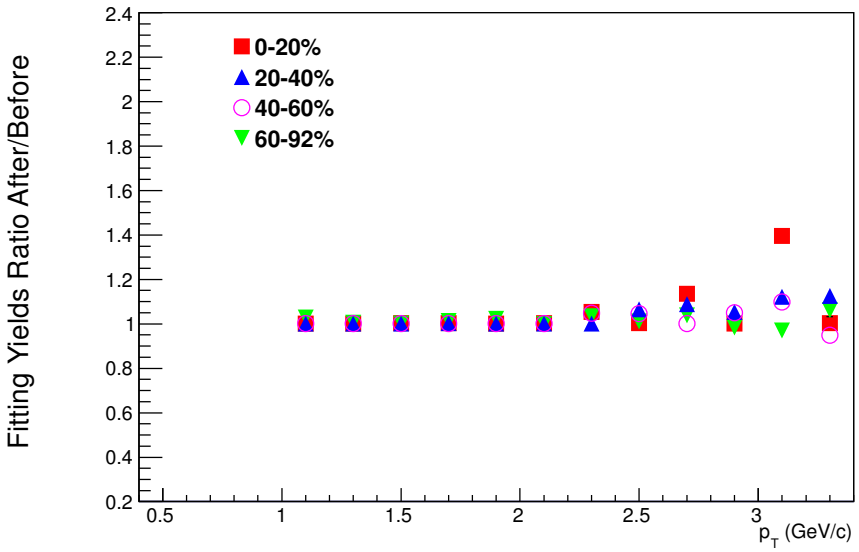


Figure 52: Background fit function systematic check.
The background fit function is changed from $F_{background}$ (4) to $A + \frac{B}{x} + \frac{C}{x^2}$ and we take this in ratio with the original yields. It would seem the extra terms don't add a massive amount to the fitting, as the variation where statistics are reasonable is nearly negligable.

In Fig.53 we plot the ratio of our yield before and after the range of the fit function has been altered by 10%. The associated systematic uncertainty is 5%.

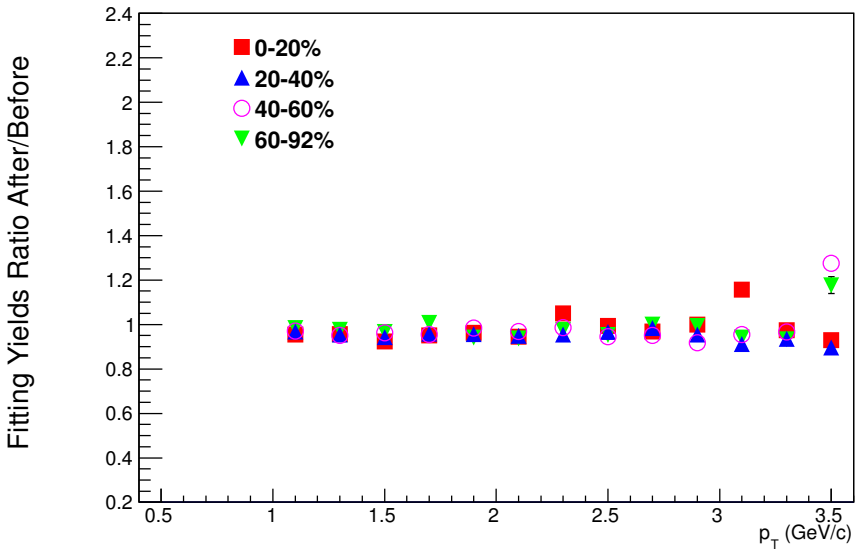


Figure 53: Fit function alteration systematic check.
Here the fitting function used to extract the yield is adjusted by 10% in the fitting range and a after/before ratio is plotted. The fit is sensitive to this change in particular because the background shape has a curving shape to it, so the less of the curve you include the more the fit tends to flatten out.

In Fig.54 we plot the ratio of the yields as seen in $+-$ and $-+$ field configurations using the same analysis methods. For the $p_T$ region below roughly 3 GeV/c the variations due to statistics and fitting errors is minimal and we can extract an associated systematic uncertainty of 10%.

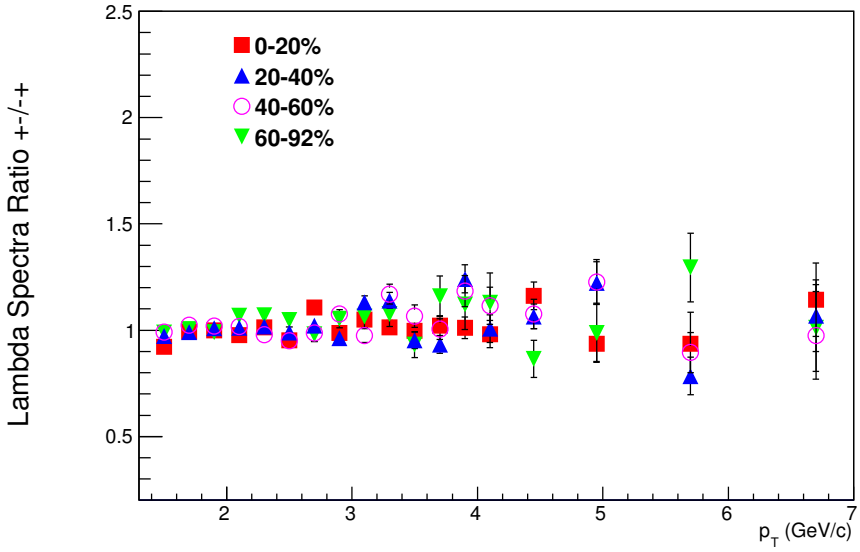


Figure 54: The ratio between the $+-$ field configuration and the $-+$ field configuration using the NoPID analysis method.

The effect of varying the track-matching residuals has an associated uncertainty of 12%. Finally, the systematic uncertainty associated with the embedding correction is set, per centrality bin, at 0.2 (1-$\epsilon_{embed}$).

Taking the results and pairing the fit extraction methods as well as the methods consistency plots as in the same class of systematic (and therefore $\sqrt{\frac{1}{N}(\epsilon_1^2+\epsilon_2^2)}$ ) the total systematic error on a given point is $\sqrt{[0.2(1-\epsilon_{embed})]^2+0.1652^2}$.

### 3.5 Unfolding

In PHENIX, our tracking algorithms assume every particle to have originated from the reconstructed collision vertex. Due to time dilation at the relativistic speeds of particles emerging from the collision, the lambda may travel many centimeters away from the original vertex before decay and the reconstructed momentum of each daughter particle may be offset from the true value. When the measured momentum of decay products is not accurate, the reconstructed momentum of a given lambda

is similarly affected, resulting in a smearing of the true $p_T$ distribution. Most of the measurements at PHENIX and other detectors will have similar resolution effects for the $p_T$-axis, but will not be large enough to affect the measured spectra in a statistically significant way. When the $\sigma$ of the $p_T$ smearing grows larger than the intended bin-width of the data it becomes necessary to make corrections for this effect [36]. For the lambda spectra as measured in PHENIX, we estimate the size of the momentum smearing in simulation and conclude that corrections are in fact needed. The distribution of reconstructed $p_T$ generated by our analysis compared to the truth generated by the simulation is shown in Fig.55.

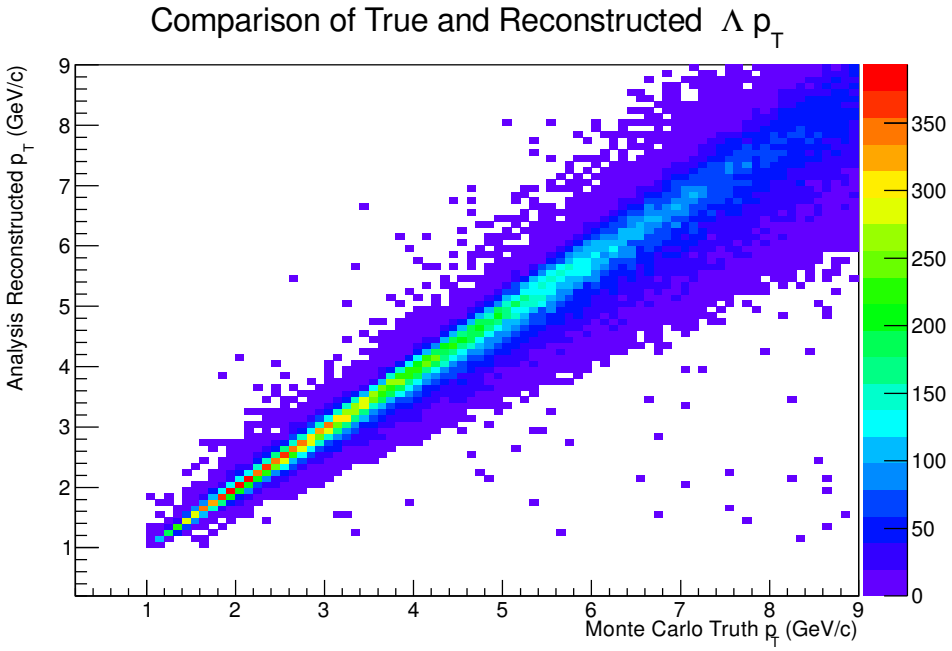


Figure 55: Single-particle simulation showing the distribution of reconstructed $\Lambda p_T$ as seen in our analysis compared to the true simulation-generated $p_T$.
At higher $p_T$ the lambda baryon is capable of traveling further before decay, meaning that the reconstructed momentum may be further away from the truth.

Generally, the problem of converting a measured distribution with inherent errors to a true distribution is known as an inverse problem and may be represented as $f'(y) = \int A(y,x)f(x)dx$, where $f'(y)$ is the measured distribution, $f(x)$ is the true

distribution, and $A(y, x)$ is the effect of the measurement process [37]. Methods for the solution of this type of problem have been studied at length in the past and a class of routines known as unfolding have been developed [38,39,40]. Specifically, for a numerical solution to the inverse problem, the integral relation above may be represented by the matrix relation $y = Ax$, where $y$ is the measured distribution in vector form, $x$ is the true distribution vector, and $A$ is the matrix that represents the smearing introduced by the measurement. Software packages have been developed and made available for the proper handling of the solution to the inverse problem described, and we have used the RooUnfold package for its seamless integration into ROOT, the PHENIX collaboration's analysis software of choice [41].

Within RooUnfold are a number of separate methods that handle the solution of the $y = Ax$ problem and are described at length in [41]. We have used the RooUnfoldBayes method, which uses an iterated application of Bayes' theorem in order to determine the appropriate response matrix for unfolding. In practice, we use single-particle simulation data to give the software a true input distribution and a measured distribution with the measurement errors, essentially the distribution in Fig.55; from this the software constructs a response matrix that may be inverted and applied to the real data in order to determine the true spectra distribution. Because one cannot assume that the simulation perfectly matches the reality of the errors in the measurement process, the unfolding is iterated in the software using real data to converge toward a true result. The RooUnfoldBayes method does not include a smoothing routine, included in other methods, to reduce the exaggeration of small statistical fluctuations, so the final unfolding result is fit with a function, rather than applying the result point-by-point. The fit function is varied and the differences are included as a systematic uncertainty.

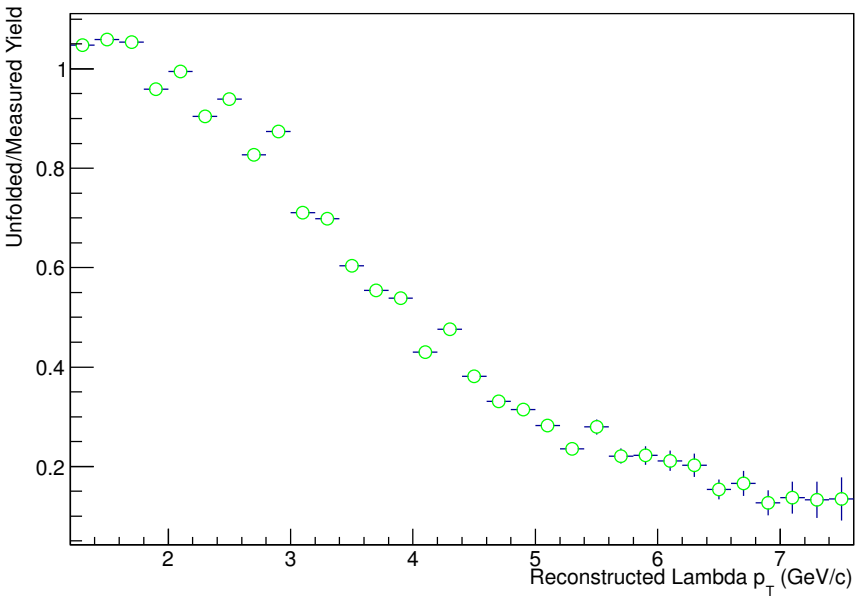


Figure 56: The RooUnfoldBayes result, given 4 iterations.
The unfolding result is fit piece-wise with gaussian distributions, 1.5-4.0 GeV/c and 4.0-7.0 GeV/c, which are then used to modify the measured spectra.

# CHAPTER 4

# RESULTS AND DISCUSSION

## 4.1 Invariant Yield and Methods Comparison

The fundamental measurement of the $\Lambda$ baryon analysis is the invariant yield as a function of transverse momentum $p_T$, separated into centrality classes. All other physics information in this analysis is derived from the invariant yield measurement. As a brief reminder, each data point represents a reconstructed lambda peak in invariant mass, which was constructed from the measured kinematic information of the lambda baryon's daughter particles. Each reconstructed lambda mass peak is fit and the integrated yield of the fit is taken as the raw yield per bin. The raw yield is further adjusted by a duplicate analysis run over simulated data in order to correct for the effects of detector efficiencies, acceptance, and occupancy. This corrected result is finally adjusted once more using unfolding methods in order to account for $p_T$ smearing introduced through tracking algorithms, which incorrectly assume particles to have originated from the collision vertex. The resulting invariant yield is presented for the $\Lambda$ and $\bar{\Lambda}$ baryons in centrality classes 0-20%, 20-40%, 40-60% and 60-92% in Fig.57. It is worth noting that the contributions from particles that feed into to the $\Lambda$ spectrum, such as $\Xi$, $\Sigma$ and $\Omega$, are not subtracted from the invariant yield, as PHENIX has no yield measurements for those primary particles. The $\Lambda$ yield with feed-down contributions is considered "inclusive" and we refrain from making physics claims that could be impacted by these effects.

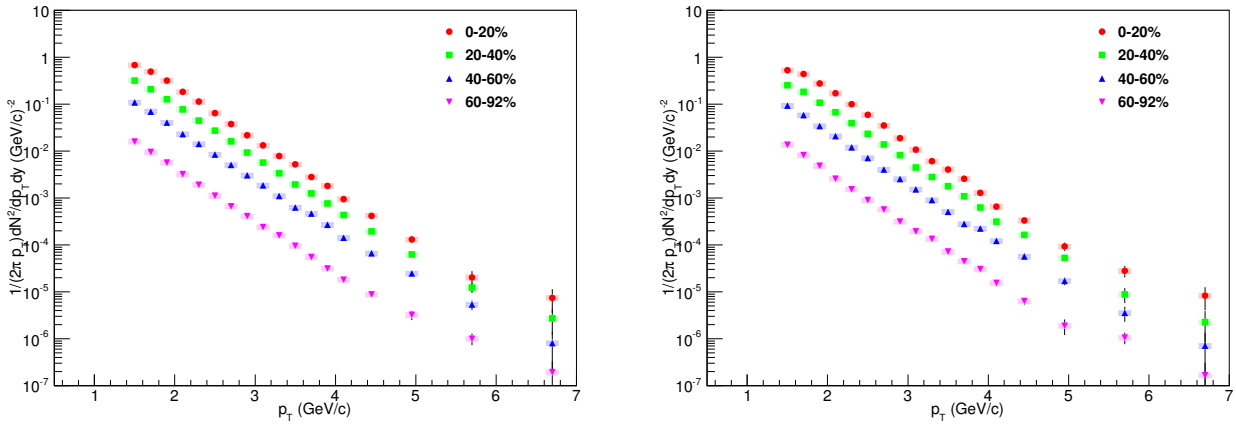


Figure 57: Inclusive invariant yield results for $\Lambda$ (left) and $\bar{\Lambda}$ (right), as a function of $p_T$, for Au+Au collisions at $\sqrt{S_{NN}} = 200$ GeV.
Presented results use the reconstruction method requiring no daughter particle identification.

Utilizing the excellent particle identification capabilities of the TOF-W, the analysis process is repeated with an additional single-leg PID requirement. The secondary method was included to evaluate the accuracy of the main result and provide systematic uncertainty constraints. The additional particle identification requirement produces peaks with fewer irregularities in the mixed-event background, potentially leading to more accurate yield results. However, while evaluating the systematic uncertainties for the PID method, we discovered that the tracking variables for the TOF-W in our simulation do not match the behavior observed in real data for our analysis specifically. The TOF-W has been used to great effect in other analyses looking at tracks originating from the reconstructed collision vertex and so we attribute this discrepancy to the large displacement of lambda decays from the collision vertex. An accurate study of the displaced-vertex decays on the TOF-W tracking in real data would be necessary to properly account for the observed tracking discrepancy and as of the data collected for this analysis PHENIX had no way of determining a secondary vertex away from the original collision. The result is an additional 15% systematic uncertainty placed on the TOF-W PID-method yield.

The two analysis methods may still be compared and are seen to be in good agreement, within uncertainties. There is a clear rise in their ratio, as seen in Fig.58, but the increased TOF-W PID-method uncertainties prevent us from making further claims on the accuracy of the main result.

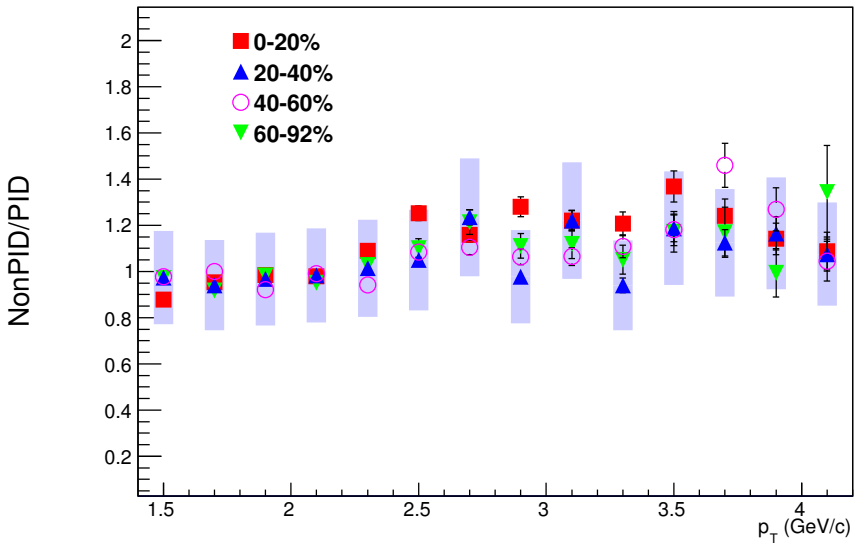


Figure 58: Ratio of invariant yield non-PID to PID method
While there is a rising slope when comparing the two methods, the results remain within statistic and systematic uncertainties.

Beyond the comparison of our own methods, the $\Lambda$ baryon was previously measured by the STAR collaboration for the same collision species and energy. Our result must be compared to previously published measurements and we must address any discrepancies between them. The data published by STAR in Ref. [28] was produced using different binning from our current study, and so we are unable to make point-to-point comparisons. Instead, we fit the STAR data with the tsallis function, $f_{tsallis}(p_T) = \frac{1}{2\pi}\frac{dN}{dy}\frac{(n-1)(n-2)}{nT(nT+m_0(n-2))}\left[1+\frac{m_T-m_0}{nT}\right]^{-n}$, and compare our data points to those fits. The fits are varied, and the differences between fit and STAR data are used as an additional source of systematic uncertainty, 5% added in quadrature with the previously determined systematic uncertainties. Additionally, the STAR data is

published in 0-5% and 10-20% centrality classes, rather than our own 0-20% class. A comparison can be drawn using their combined 0-5% and 10-20% data sets, but the comparison to 0-20% does not hold to higher $p_T$, where the spectral shape begins to change more rapidly between centrality classes, as seen in the nuclear modification factor $R_{CP}$, discussed later. We include the combined 0-5%, 10-20% class compared to 0-20% until 4 GeV/c. STAR data are feed-down corrected with a flat ∼15% correction [28]. For the sake of comparison, the same 15% is included as a correction to our data here, but not retained outside of this comparison.

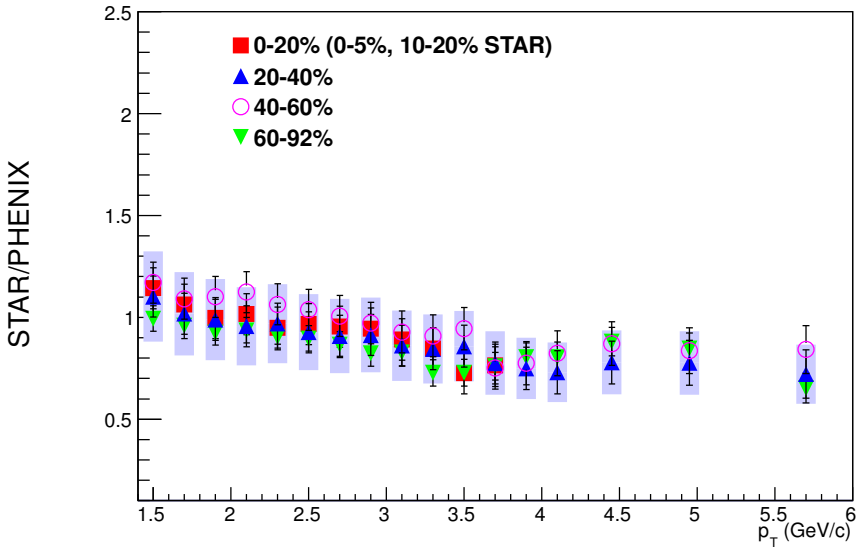


Figure 59: Comparison of the no-PID result to previously published Λ spectra by the STAR collaboration
The two results differ in the binning of the presented data, so a comparison is made using fits to the STAR spectra [28]. Appropriate systematic uncertainties arising from this method are calculated by varying fits and comparing their accuracy with the STAR data itself. As well, the STAR results were published in 0-5% and 10-20% centrality classes; our 0-20% class is compared to the combined 0-5% and 10-20% classes up to 4 GeV/c.

Our results compare well with the published STAR data, though there is a systematic falling trend in the ratio. The ratio falls over $p_T$, yet remains consistent with unity when considering statistic and systematic uncertainties. We must consider our

results to be in agreement; our systematic uncertainties would need to improve considerably in order to make a claim that our result differs quantitatively. The equivalent analysis done in the STAR detector has the capability of determining each displaced decay vertex, thereby avoiding one of the greatest challenges present in our own study.

## 4.2 Nuclear Modification Factor $R_{CP}$ and Hadronization

As described in the introduction, particle production in the hot dense medium of the QGP is not represented by a binary scaling of many individual collisions, scaled by the number of those collisions $N_{coll}$. Instead, the fireball modifies the produced spectra through in-medium energy loss interactions and a fundamental transition that includes particle production by parton recombination rather than pure fragmentation [42]. Common tools for evaluating the in-medium effects are the nuclear modification factors $R_{AA}$ and $R_{CP}$. The $R_{AA}$ requires an invariant yield measurement from a p+p collision system that we have not measured, but the $R_{CP}$ is constructed from our Au+Au $\Lambda$ yield directly. Again, $R_{CP}$ is defined as the invariant yield in the most central class divided by the most peripheral, scaled by the number of binary nucleon-nucleon collisions, $R_{CP} = \frac{Y_{central}}{Y_{peripheral}} \frac{N_{coll}^{peripheral}}{N_{coll}^{central}}$. The $R_{CP}$ for the $\Lambda$ baryon is plotted in Fig.60 for both analysis methods; systematic uncertainties accompany the NoPID method. The two methods are consistent within uncertainties and show no apparent suppression of $\Lambda$ production over intermediate $p_T$ $\sim$1.8-4.0 GeV/c.

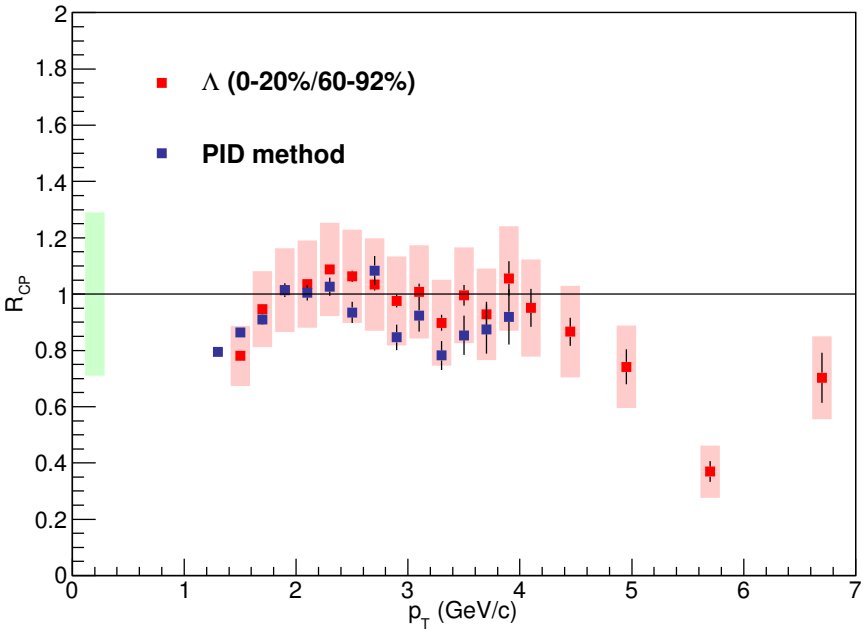


Figure 60: Nuclear modification factor $R_{CP}$ for combined +- and -+ analyses; PID and NoPID analysis methods
The green shaded bar at low $p_T$ indicates uncertainty in $N_{coll}$ as calculated using the Glauber Model.

To put this nuclear modification factor in context with other measurements, the $R_{CP}$ is plotted again in Fig.61 along with the $\phi$-meson [43] and charge-averaged protons and pions [35].

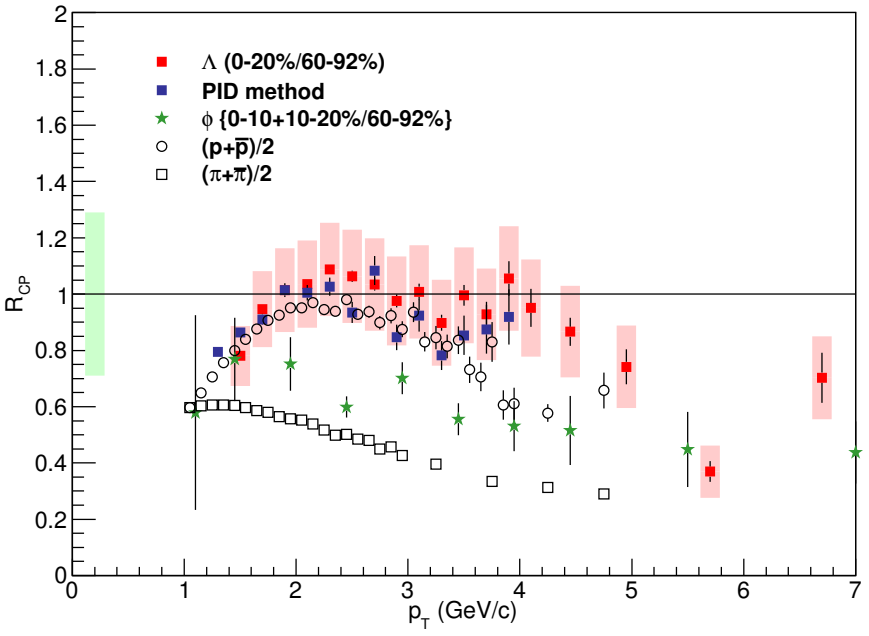


Figure 61: Nuclear modification factor $R_{CP}$, for $\Lambda$, $\phi$, and charge-averaged $p$ and $\pi$. The green shaded bar at low $p_T$ indicates uncertainty in $N_{coll}$ as calculated using the Glauber Model.

In the framework of recombination models [44, 45, 46], the $\Lambda$ baryon is expected to follow the proton's pattern of suppression given the momentum contribution from three valence quarks upon coalescence. By contrast, both the $\pi$ and $\phi$ mesons are relatively suppressed for a given $p_T$, having momentum contributions from only two valence quarks, regardless of the similar mass of the $\phi$ and proton. While this is the observed trend, indicating similar production and energy-loss characteristics for the two baryons, we note that the $\Lambda$ $R_{CP}$ remains near unity to higher $p_T$ than the protons. Strange quarks in the QGP are thermally produced from $gg \rightarrow s\bar{s}$ processes in great abundance as their mass is comparable to the critical temperature [42, 47, 48]. Within the Hwa, Yang recombination model, the $\Lambda$ baryon is produced by thermal (T) and shower (S) quark contributions, where a shower quark is a fragmenting parton, which then recombines with thermal partons to hadronize [49]. In that model, $\Lambda$ production is dominated by pure thermal, TTT, processes to roughly $p_T \approx 4.0$ GeV/c, after

which TTS processes become increasingly important, where two quarks are thermally produced and recombine with a single shower quark. Proton production, by contrast, has greater contributions from TTS and TSS processes at intermediate transverse momentum and [49] notes that by $p_T \approx 4$ GeV/c, the strength of all contributions with thermal components are roughly equivalent. With this in mind, it is reasonable to expect the $\Lambda$ baryon to display less suppression to higher $p_T$, as is observed.

Finally, we also plot the $\bar{\Lambda}/\Lambda$ ratio in Fig.62 and find it to be in good agreement to previously measured STAR (0.79±0.10, [28]) and PHENIX (0.75±0.09, [21]) results. We find the ratio to be roughly flat over $p_T$, in contrast to early predictions that expected a falling ratio, based on fragmentation and subsequent energy-loss in the medium due to gluon bremsstrahlung [50]. This result further supports the notion of particle production mechanisms beyond fragmentation like those presented in recombination models.

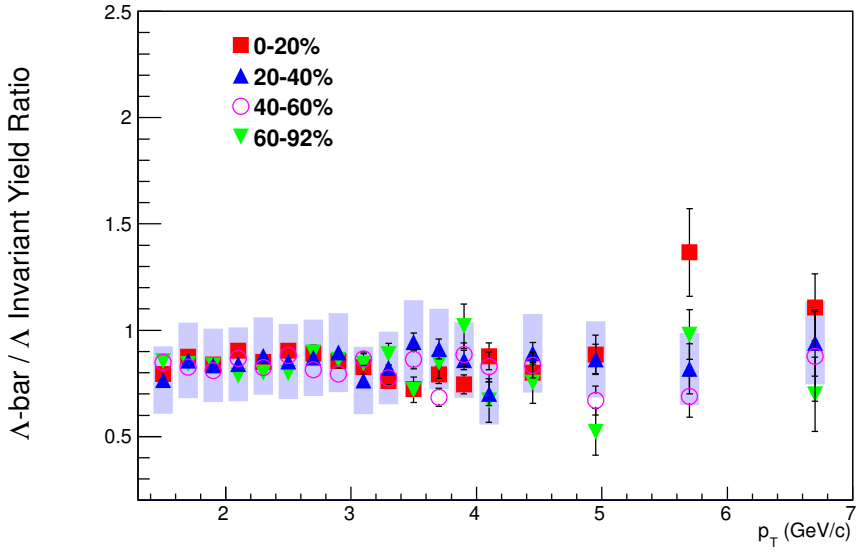


Figure 62: Ratio comparing the invariant yield of $\Lambda$ and $\bar{\Lambda}$.
The average value is consistent with previous measurements done by STAR and PHENIX and is roughly flat in $p_T$.

# CHAPTER 5

## SUMMARY

We have presented inclusive $\Lambda$ and $\bar{\Lambda}$ spectra for the Au+Au collision system at $\sqrt{S_{NN}}$ = 200 GeV for the range 1.5 GeV/c $< p_T <$ 7 GeV/c. Our results are consistent, within uncertainties, with a previous measurement done by STAR [28] and support previous $\bar{\Lambda}/\Lambda$ ratios. As well, our $R_{CP}$ result sheds light on energy loss and particle production mechanisms in the QGP that supports the recombination models including thermal strange-quark production as the dominant mechanism to roughly 4.0 GeV/c in transverse momentum. We have further demonstrated that it is possible to correct for inaccurate momentum reconstruction in PHENIX through the use of unfolding routines, which we believe have not previously been used in PHENIX analyses.

No analysis is perfect and our $\Lambda$ baryon measurement can be improved at PHENIX should the topic be revisited in other data sets. The two most important challenges to address are the mis-reconstruction of displaced decay vertices and the accurate measure of feed-down contamination from $\Xi$, $\Omega$, and $\Sigma$ particle families. While we have addressed the first issue raised with the application of unfolding methods, the most direct and accurate method is the determination of a the secondary vertex of a given decay, thereby eliminating the inaccuracies introduced by assuming each track came from the original collision vertex. This is the approach taken by STAR and more recent results from LHC-era detectors such as ALICE [56]. Not only does the accuracy of a given track reconstruction improve, but the background is dramatically reduced for the invariant mass yield extraction, as seen in Fig.63 taken from the ALICE result [56].

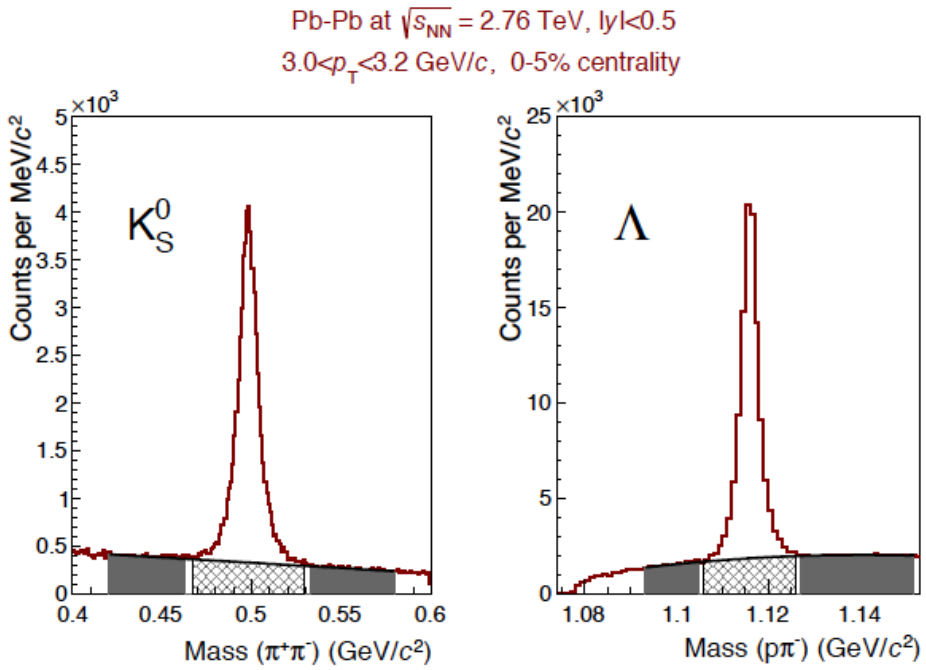


Figure 63: Lambda invariant mass peak reconstructed by ALICE, benefitting from identified secondary vertex cut [56]

Some years after the data acquired in 2007 for our presented analysis, PHENIX has installed a new detector named the silicon vertex tracker (SVTX) [57], which is able to better determine the secondary vertex decay of a track. While we acknowledge that the multiplicity in central Au+Au collisions may be too high for use of this new detector in $\Lambda$ analyses, it may certainly prove useful in baseline p+p and d+Au measurements, as well as more peripheral Au+Au and Cu+Cu systems. If the SVTX is able to improve the $\Lambda$ measurement, it may also be reasonable to attempt reconstruction of $\Xi^- \rightarrow \Lambda + \pi^-$ and $\Xi^+ \rightarrow \bar{\Lambda} + \pi^+$, making it possible to provide an accurate feed-down estimate for the $\Xi$ particle family using PHENIX data, the dominant source of contamination in the $\Lambda$ invariant yield [28, 56].

With properly feed-down corrected spectra we would be able to expand the physics message derived from the measurements presented here. Notably, it would be possible to verify the $\Lambda/p$ ratio of ~0.9 and the $\bar{\Lambda}/\bar{p}$ ratio of ~0.95 as measured by Refs. [24,

26] as well as the $\Lambda/K^0_S$ ratio shown in Fig.64, which is sensitive to baryon/meson production mechanisms with the added strangeness content information. These ratios and their $p_T$ behavior provide valuable constraints for models looking to reproduce the behaviors observed in the produced QGP. PHENIX has published spectra for $K^0_S$ in p+p, d+Au, and Cu+Cu previously [58]. The addition of a $K^0_S$ measurement in Au+Au collisions at PHENIX along with the suggested improvements to the analysis presented here would provide valuable additions to the field.

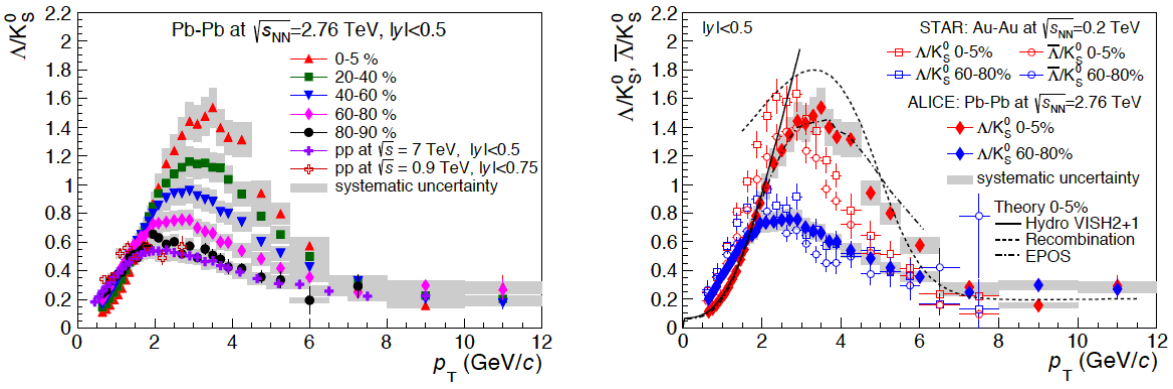


Figure 64: $\Lambda/K^0_S$ as presented in Ref.[56]
This ratio is sensitive to baryon/meson production mechanisms for particles with strangeness content.

## References


[1] E. Fermi, High Energy Nuclear Events. Prog. Theor. Phys. 5, 570 (1950)

[2] I. Pomeranchuk, Proceedings of USSR Academy of Sciences 78, 889 (1951)

[3] R. Hagedorn, Statistical Thermodynamics of Strong Interactions at High Energies. Suppl. Nuovo Cimento 3, 147 (1965)

[4] R. Hagedorn, On the Hadronic Mass Spectrum. Nuovo Cimento 52:1336-1340 (1967)

[5] J. C. Collins and M. J. Perry, Superdense Matter: Neutrons or Asymptotically Free Quarks? Phys. Rev. Lett. 34, 1353 (1975)

[6] C. N. Yang and R. L. Mills, Conservation of Isotopic Spin and Isotopic Gauge Invariance. Phys. Rev. 96, 191 (1954)

[7] D. J. Gross and F. Wilczek, Asymptotically Free Gauge Theories. Phys. Rev. D 8, 3633 (1973)

[8] *É*. V. Shuryak, Theory of Hadronic Plasma. Zh. Eksp. Teor. Fiz. 74: 408-420 (1978)

[9] F. Karsch, Lattice QCD at High Temperature and Density. Lect. Notes Phys. 583, 209 (2002)

[10] Private PHENIX Web Archive

[11] K. Adcox *et al.*, Formation of Dense Partonic Matter in Relativistic Nucleus-Nucleus Collisions at RHIC: Experimental Evaluation by the PHENIX Collaboration. nucl-ex/0410003v3 (2005)

[12] J. D. Bjorken, Highly Relativistic Nucleus-Nucleus Collisions: The Central Rapidity Region. Phys. Rev. D 27, 140 (1983)

[13] D. Teaney, J. Lauret, E. V. Shuryak, A Hydrodynamic Description of Heavy Ion Collisions at the SPS and RHIC. nucl-th/0110037 (2001)

[14] P. Huovinen, P. F. Kolb, U. W. Heinz, P. V. Ruuskanen, S. A. Voloshin, Radial and Elliptic Flow at RHIC: Further Predictions. Phys. Lett. B503, 58 (2001)

[15] P. F. Kolb, R. Rapp, Transverse Flow and Hadro-Chemistry in Au+Au Collisions at $\sqrt{S_{NN}} = 200$ GeV. Phys. Rev. C67:044903 (2003)

[16] A. Adare et al., Scaling Properties of Azimuthal Anisotropy in Au+Au and Cu+Cu Collisions at $\sqrt{S_{NN}} = 200$ GeV. Phys. Rev. Lett. 98:162301 (2007)

[17] M. Kaneta, N. Xu, Centrality Dependence of Chemical Freeze-out in Au+Au Collisions at RHIC. nucl-th/0405068 (2004)

[18] Prashant Shukla, Glauber Model for Heavy Ion Collisions from Low Energies to High Energies. nucl-th/0112039 (2001)

[19] S. S. Adler *et al.*, High-pT Charged Hadron Suppression in Au+Au Collisions at $\sqrt{S_{NN}}$ = 200 GeV. Phys. Rev. C69:034910 (2004)

[20] S. S. Adler *et al.*, Production of Phi mesons at mid-rapidity in $\sqrt{S_{NN}}$ = 200 GeV Au+Au Collisions at RHIC, Phys. Rev. C 72, 014903(2005)

[21] R. J. Fries, B. Müller, C. Nonaka, and S. A. Bass, Hadronization in Heavy-Ion Collisions: Recombination and Fragmentation of Partons, Phys. Rev. Lett. 90, 202303 (2003)

[22] R. C. Hwa and C. B. Yang, Recombination of Shower Partons at High $p_T$ in Heavy-Ion Collisions. Phys. Rev. C70:024905 (2004)

[23] S. S. Adler *et al.*, Suppressed $\pi^0$ Production at Large Transverse Momentum in Central Au+Au Collisions at $\sqrt{S_{NN}}$ = 200 GeV. Phys. Rev. Lett. 91:072301 (2003)

[24] K. Adcox *et al.*, Measurement of the $\Lambda$ and $\bar{\Lambda}$ particles in Au+Au Collisions at $\sqrt{S_{NN}}$ = 130 GeV. nucl-ex/0204007 (2002)

[25] B. I. Abelev *et al.*, Measurements of Strange Particle Production in p+p Collisions at $\sqrt{S_{NN}}$ = 200 GeV. nucl-ex/0607033v1 (2006)

[26] J. Adams *et al.*, Scaling Properties of Hyperon Production in Au+Au Collisions at $\sqrt{S_{NN}}$ = 200 GeV. nucl-ex/0606014v1 (2006)

[27] J. Adams *et al.*, Proton-Lambda Correlations in Central Au+Au Collisions at $\sqrt{S_{NN}}$ = 200 GeV. nucl-ex/0511003 (2006)

[28] G. Agakishiev *et al.*, Strangeness Enhancement in Cu+Cu and Au+Au Collisions at $\sqrt{S_{NN}}$ = 200 GeV. Phys. Rev. Lett. 108, 072301 (2012).

[29] M. Allen et al., PHENIX Inner Detectors. Nucl. Instrum. Meth., A499:549-559 (2003)

[30] K. Adcox et al., PHENIX Central Arm Tracking Detectors. Nucl. Instrum. Meth., A499:489-507 (2003)

[31] J. Barrette et al., The Pixel Readout System for the PHENIX Pad Chambers. Nucl. Instrum. Meth., A661:665-668 (1999)

[32] B. Love et al., The Implementation and Performance of the PHENIX Time-of-Flight West Detector Subsystem.

[33] Akio Kiyomichi *et al.*, PHENIX analysis note 328 Final analysis note for phi->K+K- in Run2 Au + Au collisions (PPG016). Internal PHENIX collaboration documentation.

[34] R. Belmont, PHENIX analysis note 814 Identified Charged Hadron Single Particle Spectra in Run7. Internal PHENIX collaboration documentation.

[35] A. Adare *et al.*, Spectra and Ratios of Identified Particles in Au+Au and d+Au Collisions at $\sqrt{S_{NN}}$ = 200 GeV. Phys. Rev. C 88, 024906 (2013)

[36] L. Lyons, Unfolding: Introduction. In H. B. Prosper and L. Lyons, editors, Proceedings of the PHYSTAT 2011 Workshop on Statistical Issues Related to Discovery Claims in Search Experiments and Unfolding, CERN-2011-006, pages 225–233 (2011)

[37] V. Blobel, An Unfolding Method for High Energy Physics Experiments. hep-ex/0208022 (2002)

[38] A. Hoecker and V. Kartvelishvili, SVD Approach to Data Unfolding. Nucl. Instrum. Meth. A372:469-481 (1996)

[39] S. Schmitt, TUnfold: An Algorithm for Correcting Migration Effects in High Energy Physics. arXiv:1205.6201 (2012)

[40] G. D'Agostini, Improved Iterative Bayesian Unfolding. arXiv:1010.0632 (2010)

[41] T. Adye, Unfolding Algorithms and Tests Using RooUnfold. arXiv: 1105.1160 (2011)

[42] J. Rafelski and B. Müller, Strangeness Production in the Quark-Gluon Plasma. Phys. Rev. Lett. 48, 1066 (1982)

[43] A. Adare *et al.*, Nuclear Modification Factors of Phi Mesons in d+Au, Cu+Cu and Au+Au collisions at $\sqrt{S_{NN}}$ = 200 GeV. Phys. Rev. C 83, 024909 (2011)

[44] V. Greco, C. M. Ko, and P. Lévai, Parton Coalescence and the Antiproton/Pion Anomaly at RHIC. Phys. Rev. Lett. 90, 202302 (2003)

[45] R.C. Hwa and C.B. Yang, Scaling Behavior at High $p_T$ and the p/pi Ratio. Phys. Rev. C 67, 034902 (2003)

[46] R. J. Fries, B. Müller, C. Nonaka, and S. A. Bass, Hadron Production in Heavy Ion Collisions: Fragmentation and Recombination from a Dense Parton Phase. Phys. Rev. C 68, 044902 (2003)

[47] M. M. Aggarwal *et al.*, Strange and Multi-strange Particle Production in Au+Au Collisions at $\sqrt{S_{NN}}$ = 62.4 GeV. Phys. Rev. C 83, 024901 (2011)

[48] R.C. Hwa and C.B. Yang, Strangeness Enhancement in the Parton Model. Phys. Rev. C 66, 064903 (2002)

[49] R.C. Hwa and C.B. Yang, Production of Strange Particles at Intermediate $p_T$ at RHIC. Phys. Rev. C 75, 054904 (2006)

[50] X.N. Wang, Effect of Jet Quenching on High $p_T$ Hadron Spectra in High-Energy Nuclear Collisions. Phys. Rev. C 58, 2321 (1998)

[51] H. Hahn *et al.*, The RHIC Design Overview. Nucl. Instrum. Meth., A499:245-263 (2003)

[52] K. Adcox *et al.*, PHENIX Detector Overview. Nucl. Instrum. Meth., A499:469-479 (2003)

[53] K. Ikematsu *et al.*, A Start-Timing Detector for the Collider Experiment PHENIX at RHIC-BNL. *Nucl. Instrum. Meth.*, A411:238-248 (1998)

[54] V. G. Ryabov, Drift Chambers for the PHENIX Central Tracking System. *Nucl. Instrum. Meth.*, A419:363-369 (1998)

[55] H. D. Politzer, Reliable Perturbative Results for Strong Interactions? Phys. Rev. Lett. 30, 1346 (1973)

[56] B. Abelev *et al.*, $K^0_S$ and $\Lambda$ Production in Pb-Pb Collisions at $\sqrt{S_{NN}} = 2.76$ TeV. Phys. Rev. Lett. 111, 222301 (2013)

[57] T. Hachiya, PHENIX Silicon Vertex Tracker (VTX), Focus Seminar. www.phenix.bnl.gov/phenix/WWW/intro/detectors/focus/focus_vtx.pdf (2011)

[58] A. Adare *et al.*, Measurement of $K^0_S$ and $K^{*0}$ in $p$+$p$, $d$+Au and Cu+Cu collisions at $\sqrt{S_{NN}}$= 200 GeV. nucl-ex:1405.3628 (2014)

[59] N. Herrmann, J. P.Wessels, and T.Wienold, Collective Flow in Heavy-Ion Collisions. Ann. Rev. Nucl. Part. Sci., 49:581 (1999)